The Astrophysical Journal, 956:70 (26pp), 2023 October 20 https://doi.org/10.3847/1538-4357/acf6b5

The Evaporating Massive Embedded Stellar Cluster IRS 13 Close to Sgr A*. I. Detection of a Rich Population of Dusty Objects in the IRS 13 Cluster

Florian Peißker[1], Michal Zajaček[2], Lauritz Thomkins[1], Andreas Eckart[1,3], Lucas Labadie[1], Vladimír Karas[4], Nadeen B. Sabha[5], Lukas Steiniger[1], and Maria Melamed[1]
[1] I.Physikalisches Institut der Universität zu Köln, Zülpicher Str. 77, D-50937 Köln, Germany; peissker@ph1.uni-koeln.de
[2] Department of Theoretical Physics and Astrophysics, Faculty of Science, Masaryk University, Kotlářská 2, 611 37 Brno, Czech Republic
[3] Max-Plank-Institut für Radioastronomie, Auf dem Hügel 69, D-53121 Bonn, Germany
[4] Astronomical Institute, Czech Academy of Sciences, Boční II 1401, CZ-14100 Prague, Czech Republic
[5] Institut für Astro- und Teilchenphysik, Universität Innsbruck, Technikerstr. 25, A-6020 Innsbruck, Austria
Received 2023 July 13; revised 2023 August 22; accepted 2023 August 23; published 2023 October 10

Abstract

A detailed analysis of the nuclear star cluster not only concedes the existence of the S cluster, with its fast-moving stars and the supermassive black hole Sgr A*. It also reveals an embedded region of gas and dust with an exceptionally high stellar density called IRS 13. The IRS 13 cluster can be divided into the northern and eastern counterparts, called IRS 13N and IRS 13E, respectively. This work will focus on both regions and study their most prominent members using rich infrared and radio/submillimeter data baselines. Applying a multiwavelength analysis enables us to determine a comprehensive photometric footprint of the investigated cluster sample. Using the ray-tracing-based radiative transfer model HYPERION, the spectral energy distribution of the IRS 13 members suggests a stellar nature of the dusty sources. These putative young stellar objects (YSOs) have a comparable spectroscopic identification to the D and G sources in or near the S cluster. Furthermore, we report the existence of a population of dusty sources in IRS 13 that can be mostly identified in the *H*, *K*, and *L* band. We propose that, together with the objects reported in the literature, this population is the outcome of a recent star formation process. Furthermore, we report that these presumably young objects are arranged in a disk structure. Although it cannot be excluded that the intrinsic arrangement of IRS 13 does show a disk structure, we find indications that the investigated cluster sample might be related to the counterclockwise disk.

Unified Astronomy Thesaurus concepts: Supermassive black holes (1663); Galactic center (565); Young stellar objects (1834); Young massive clusters (2049); Intermediate-mass black holes (816)

Supporting material: figure set, machine-readable tables

1. Introduction

The bright and variable radio source Sgr A*, identified as the supermassive black hole (SMBH), is at the center of the nuclear star cluster (NSC; Menten et al. 1997; Eckart et al. 2017; Tursunov et al. 2020; Genzel 2022). Sheltering a rich depot of various types of stars, the NSC in the Galactic center (GC) enables detailed studies of its structure and components (Schödel et al. 2009; Baumgardt et al. 2018; Shahzamanian et al. 2022). As a prominent substructure of the NSC, the IRS 13 cluster has drawn attention because of the possibility of hosting an intermediate-mass black hole (IMBH) with several $\sim 10^4\,M_\odot$ (see Portegies Zwart & McMillan 2002; Maillard et al. 2004; Schödel et al. 2005). Although every attempt to find such an IMBH has resulted in a dead end (see the X-ray observations in Zhu et al. 2020; Wang et al. 2020), the question remains why the embedded cluster IRS 13 seems to resist the gravitational, and consequently disruptive, influence of Sgr A* (Mužić et al. 2008). With this correlation in mind, Tsuboi et al. (2017a) analyzed the ionized gas associated with IRS 13E, showing velocities of up to several hundred km s^{-1} on a highly eccentric orbit around a central component of the cluster, namely E3 (Fritz et al. 2010). Tsuboi et al. suggested that the blue- and redshifted velocities might indicate the presence of an IMBH responsible for the circular motion of the ionized gas. Although the existence of an IMBH is disputed (Zhu et al. 2020), the IRS 13 cluster features various additional fruitful scientific topics (Paumard et al. 2006). For example, Eckart et al. (2004) investigated the population of presumably young stellar objects (YSOs) in IRS 13N. Photometric analysis of these dusty IRS 13N objects showed similarities with the D sources (also donated as G sources, see Peißker et al. 2020c; Ciurlo et al. 2020) in the S cluster (Eckart et al. 2004, 2013), suggesting a common nature. On larger scales, and in comparison with the observations of single objects such as the mentioned D sources, Lutz et al. (1993) analyzed the forbidden iron line emission in the *inner parsec* showing a bow-shock-like distribution. The strongest [Fe III] emission was located at the position of the IRS 13 cluster, which also included the region of the prominent early-type star IRS 2L (Buchholz et al. 2013; Roche et al. 2018). As we found in Peißker et al. (2020c), all the dusty objects to the west of the Brγ-bar (Schödel et al. 2011; Peißker et al. 2020b) do exhibit prominent [Fe III] lines, while the spectra of all the sources, which are located in projection to the east of the bar, do not exhibit [Fe III] emission. The basic mechanism behind this dichotomy is still under debate and may be part of a larger scientific frame (Jalali et al. 2014; Peißker et al. 2021c) that will be discussed in the upcoming publications.

A different debate accompanies the analysis of the dusty sources of the Galactic center (for an overview, see

Peißker et al. 2020c; Ciurlo et al. 2020). This discussion started with the observation of the fast-moving G2 a decade ago (Gillessen et al. 2012). While the authors of Gillessen et al. proposed a coreless cloud nature of the object, several follow-up studies questioned this classification and suggested a stellar origin to explain the emission of G2 (Murray-Clay & Loeb 2012; Scoville & Burkert 2013; Eckart et al. 2013; Zajaček et al. 2014; Shahzamanian et al. 2016; Zajaček et al. 2017). Currently, numerous authors are in favor of a stellar nature of G2, especially because of the missing flare activity of Sgr A* that was proposed for the periapse. For example, Witzel et al. (2014) showed a pointlike L-band source close to Sgr A* with no elongation. Recently, we underlined the classification of G2 as a low-mass star embedded in a dusty envelope by analyzing a large data baseline covering the epochs between 2005 and 2019 (Peißker et al. 2021c). Observations of other objects, such as X7 (Clénet et al. 2003, 2005; Mužić et al. 2010), revealed a similar nature compared with G2 (Peißker et al. 2021a). The data suggest that these dusty sources belong to a stellar subclass that shows characteristics similar to YSOs (Lada 1987). Based on observed colors of dusty sources found in IRS 13, Eckart et al. (2004) classified the investigated objects as YSOs. In this work, we will focus on the dusty sources of IRS 13, which seem to follow the same morphology as G2, X7, and the D sources (Peißker et al. 2020c, 2021c).

Based on a multiwavelength photometric analysis, we use the radiative transfer code HYPERION (Robitaille 2011) to investigate the stellar type of the dusty sources. Furthermore, we test the validity of HYPERION by analyzing the flux density distribution of IRS 3. In addition to the dusty sources found in Eckart et al. (2004), we identify 33 newly discovered objects that can be observed in the H, K, and L band. For this new population of objects, we find a similar photometric footprint compared with the literature-known dusty sources, suggesting a similar nature. Compared with a uniform cluster, IRS 13 seems to show an underlying pattern regarding the normalized angular momentum vector, which advocates a counterclockwise disk membership. However, this particular point will be investigated in detail in Paper II. In this paper, we focus on the detection and analysis of the newly discovered sources and the classification of the dusty objects. This work is structured as follows. In Section 2, we will list the used instruments and the related telescopes. We also give an overview of the used methods and tools for the analysis. Section 2 is followed by the results in Section 3, where we present the identification and the analysis of the dusty sources of the IRS 13N cluster. The results of Section 3 are discussed in Section 4. Subsequent to Section 4, we conclude the discussion in Section 5. In Appendix A, we list the used data and show supporting results of our analysis presented.

2. Data and Tools

In this section, we will introduce the instruments that were used to observe the GC and describe the applied techniques for the analysis. The publicly available archival data is listed in Appendix A.

2.1. SINFONI and NACO

The Spectrograph for INtegral Field Observations in the Near Infrared (SINFONI, Eisenhauer et al. 2003; Bonnet et al. 2004) and Nasmyth Adaptive Optics System (NAOS) Near-infrared Imager and Spectrograph (CONICA), abbreviated as NACO (Lenzen et al. 2003; Rousset et al. 2003), were mounted at the Very Large Telescope on top of Cerro Paranal, Chile. The near-infrared imager NACO operates in the H, K, L, and M band and provides a set of narrow filters. NACO is equipped with an S13, S27, and S54 camera with a related spatial pixel scale of 13.3 mas, 27.0 mas, and 54.3 mas, respectively.

Furthermore, SINFONI is capable of providing a spectrum along with the produced image because of its integrated field unit (IFU). Hence, every pixel shows a related spectrum, resulting in a 3D data cube (two spatial dimensions and one spectral dimension). The SINFONI data used here were observed in the $H+K$ band (1.4–2.4 μm) with a related pixel scale of $0\farcs1$ and a spectral resolution of 1500. Adaptive optics is enabled for both instruments. We apply common reduction steps, like the LINEARITY/DARK correction resulting in FLAT FIELDING. The prementioned reduction steps are applied to the data of both instruments. Because of the spectroscopic characteristics of SINFONI, we also use a WAVELENGTH and DISTORTION calibration. It should be noted that NACO and SINFONI have been decommissioned since 2019. As a successor, ERIS (Davies et al. 2018) combines the capabilities of NACO and SINFONI.

2.2. ALMA

The Atacama Large Millimeter/submillimeter Array (ALMA) is on the Chajnantor Plateau, in Chile. The radio and submillimeter (submm) observations can be executed between 31 and 1000 GHz. The majority of the ALMA CO data used in this work (Prog. ID: 2015.1.01080.S) have been reduced with Common Astronomy Software Applications (CASA, CASA Team et al. 2022) and analyzed and discussed in Tsuboi et al. (2017b, 2019, 2020a, 2020b). In addition, we use scientific-ready data from the ALMA archive related to the Prog. ID 2012.1.00543.S (Martín et al. 2012; Moser et al. 2017). The ALMA data discussed and analyzed in this work show CO $v=0$ (transition 3–2) at 343 GHz.

2.3. Radiative Transfer Model

For the flux analysis based on the presented multiwavelength observations, we use the radiative transfer code HYPERION[6] using dust grains as ray-tracing sources (Robitaille 2011, 2017). For the spectrum that serves as an input quantity for HYPERION, we use flux density values estimated from the magnitude of the related source. Consequently, we measure the peak counts of the object of interest and compare it with a reference source with known properties. For this, we use

$$\mathrm{mag}_{\mathrm{obj}} = \mathrm{mag}_{\mathrm{ref}} - 2.5\log\left(\frac{\mathrm{counts}_{\mathrm{obj}}}{\mathrm{counts}_{\mathrm{ref}}}\right) \quad (1)$$

where $\mathrm{mag}_{\mathrm{ref}}$ and $\mathrm{counts}_{\mathrm{ref}}$ refer to the reference source, and $\mathrm{mag}_{\mathrm{obj}}$ and $\mathrm{counts}_{\mathrm{obj}}$ to the analyzed object. We estimate the source flux with

$$f_{\mathrm{obj}} = f_{\mathrm{ref}} \times 10^{[-0.4(\mathrm{mag}_{\mathrm{obj}} - \mathrm{mag}_{\mathrm{ref}})]} \quad (2)$$

where f_{ref} donates the flux (called zero flux) of the reference source. The basic settings for the code are listed in Table 1.

[6] HYPERION: an open-source parallelized 3D dust continuum radiative transfer code.

Table 1
Basic input parameters for HYPERION

Properties	Setting
Number of Photons	10^4
Ray-tracing Sources	10^2
Number of Iterations	10

Note. Additional parameters for the model are listed in Section 3. To optimize the computational time for the investigated cluster members, we reduce the number of photons and ray-tracing sources by two orders of magnitude compared with the model results discussed in Peißker et al. (2023b). Because of the low coverage of the spectral distribution due to the deficient amount of flux density values, the reduced number of radiators is not reflected in a significant qualitative difference.

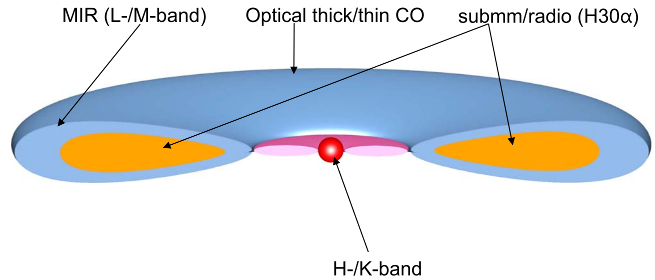

Figure 1. Sketch of a class I YSO. As indicated, various components are detectable only at specific wavelengths/bands. Using this model of a class I YSO, we expect higher luminous mid-infrared (*L/M* band) emission compared with the near-infrared (*H*/*K* band). This sketch is inspired by a similar figure shown in Sicilia-Aguilar et al. (2016).

The code allows modeling various components of YSOs, such as the gaseous accretion disk or bipolar cavities (see Figure 1 and Sicilia-Aguilar et al. 2016). For the code used in this analysis, we model a flared disk with increasing height. The shape of the flared disk is described with

$$h_{(R)} = h_0\left(\frac{R}{R_0}\right)^{\beta} \tag{3}$$

where we set $\beta = 1.25$ following the settings used in Robitaille (2011, 2017). Furthermore, a flattened rotational and infalling dust envelope (Ulrich type, see Ulrich 1976) can be modeled depending on the flux density. Because HYPERION uses grains as emitters, the properties of dust are directly related to the outcome of the model. Therefore, in the following section, we will outline the dust model used for the radiative transfer analysis. For the assumed model that is used in HYPERION, we construct a dusty envelope and a gaseous accretion disk that are arranged around a stellar core. Because of the lack of high-resolution (spectral/spatial) IFU data covering the IRS 13 region, we cannot validate or exclude the presence of bipolar cavities (an example of these cavities is displayed in Peißker et al. 2019). In summary, our assumed model resembles the composition of a class I YSO (Figure 1).

2.3.1. Dust models

The composition of dust has a particular impact on photometric studies in the GC. It is, therefore, obvious that the evolution of dust models is coupled to a precise knowledge of the different spectral species. For example, Weingartner & Draine (2001) limit their extinction law to the presence of carbonaceous and silicate grains. In contrast, the authors of Fritz et al. (2011) investigated the incorporation of many more infrared emission lines, such as CO, CO_2, aliphates, and silicates. In addition, Fritz et al. consider the presence of ice particles (H_2O and CO ice) in agreement with the studies by Moneti et al. (2001) and Moultaka et al. (2015). Fritz et al. (2011) conclude that the model of Zubko et al. (2004) is the best-fitting model to describe the extinction toward the GC. However, Zubko et al. use $R_V = A_V/E_{B-V} = 3.1$, which is consistent with the work by Draine (2003). Therefore, we use Draine (2003) to model the dust grains used in this work to perform a spectral analysis.

2.4. High-pass filter

The high-pass-filtering technique is a common tool for deblurring imaging data by minimizing the influence of the point-spread function (PSF) wings of a bright star. While the Lucy Richardson (LR) algorithm (Lucy 1974) offers a variety of setup parameters, the smooth-subtract algorithm is a robust approach to analyzing the data. Critically, the LR algorithm tends to transform elongated structures into point sources. While this does not necessarily exclude the usage of the algorithm on regions with extended structures, IRS 13 shows elongated and compact objects with unknown nature.[7] The accessible implementation into the process of analyzing the data is done by smoothing the original image $I_{\rm orig}$ with a Gaussian kernel with a size that should be in the range of the PSF measured in the data. The resulting smoothed image $I_{\rm smo}$ describes a low-pass-filtered version of $I_{\rm orig}$. With

$$I_{\rm orig} - I_{\rm smo} = I_{\rm high} \tag{4}$$

we acquire the high-pass-filtered version $I_{\rm high}$ of $I_{\rm orig}$. To enhance the image quality, one can apply a Gaussian smoothing filter smaller than the PSF to $I_{\rm high}$. A comparable description of this process is outlined in Peißker et al. (2022) as well. A rather qualitative comparison is presented in the following, where we investigate the astrometric and photometric imprint of the high-pass filter on the data. In general, we find no significant difference between a stellar position determined in $I_{\rm orig}$ or $I_{\rm high}$. For the flux shown in Figure 2, we find an uncertainty of about 20% between filtered and nonfiltered data. Taking into account the usual flux density uncertainties shown, for example, in Peißker et al. (2023b) and this work, the value distribution shown in Figure 2 is well inside the expected range. We emphasize that we expect a flux difference between high-pass-filtered and nonfiltered data due to the presence of elongated structures, such as the minispiral (see Figure 3). High-pass filtering tends to convert elongated structures into point sources, resulting in a broader flux distribution, as shown in Figure 2. Therefore, the analysis of individual sources with the high-pass filter presented here should be carried out with caution.

[7] Please see DS28 and DS33 shown in Figure 3, which form an elongated structure with α. Using the LR algorithm without the knowledge of the nature of these sources might bias the interpretation.

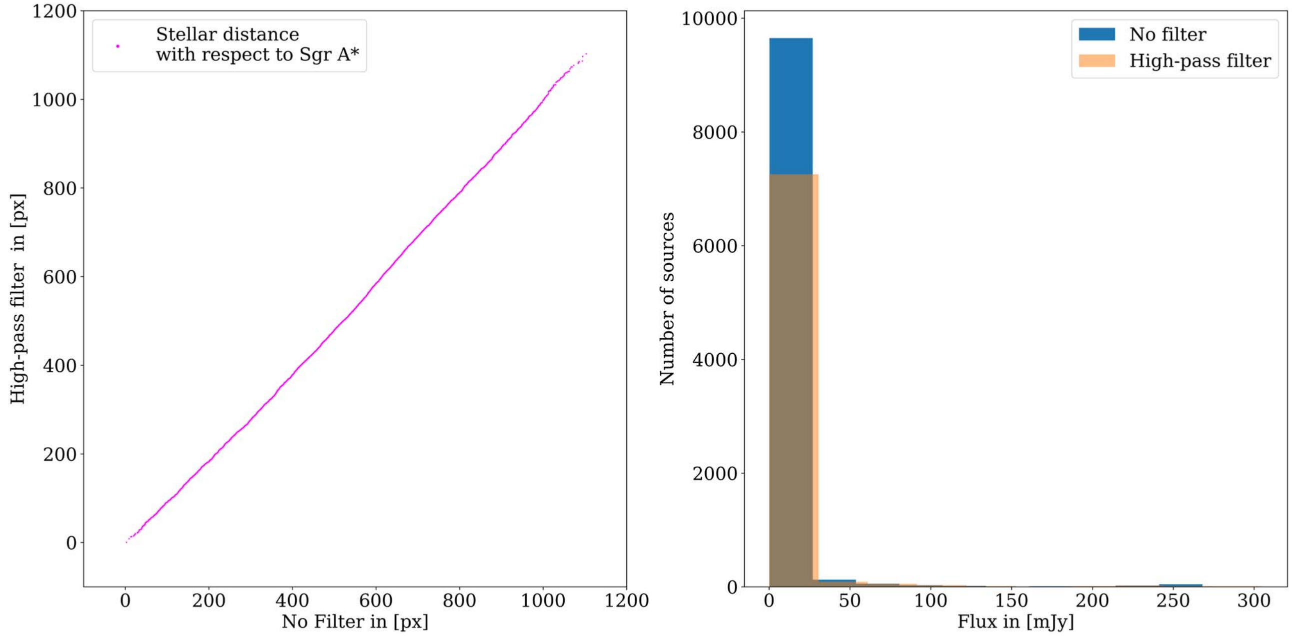

Figure 2. Comparison of raw data with processed data treated with a high-pass filter. The plot on the left shows the distance of several thousand stars with respect to Sgr A*. This plot underlines the robustness of the used high-pass filter regarding an astrometric analysis because every individual star shows the same distance to Sgr A* independent of the used approach (filter/no filter). On the right side, we show the K-band flux distribution of about 10,000 stars and estimate a difference between filtered and nonfiltered data of about 20%. Please see the text for details.

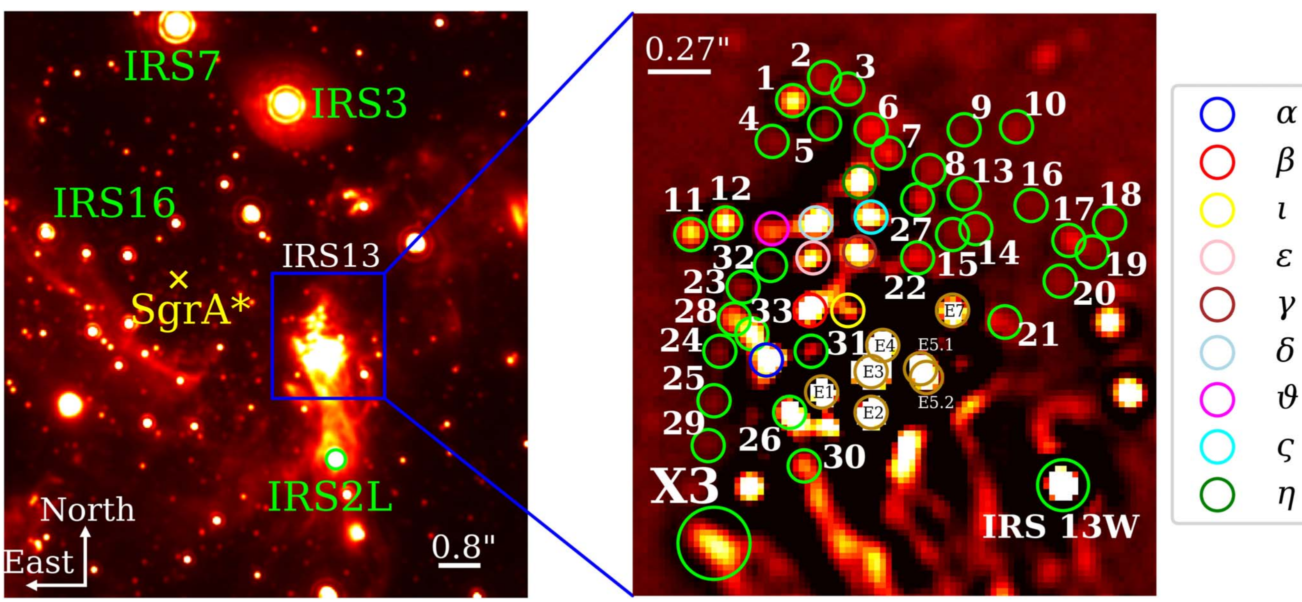

Figure 3. Finding chart for the dusty sources associated with a zoomed view toward the IRS 13 cluster. While the Greek-named sources are previously analyzed in the literature, we find additional sources that we enumerate to avoid confusion. The sources E1–E7 belong to IRS 13E and are marked for clarity. The bow-shock source X3 is analyzed in Peißker et al. (2023b). In addition, IRS 13W is associated with an M3 giant star (Maillard et al. 2004). The data shown were observed with NACO in 2004. Whereas the left image displays a continuum overview of the direct vicinity of Sgr A* (about 0.45×0.50 pc), the right represents a zoomed-in high-pass-filtered view toward IRS 13. Please consult Appendix D and Appendix E for the H- and K-band counterparts of the sources marked. In addition, Appendix F displays all newly identified dusty sources in the H, K, and L band, including their related light curve. Every source not marked in this finding chart is not considered to be a cluster member because of its proper motion or previous studies (Pfuhl et al. 2014; Gautam et al. 2019).

3. Results

In the following, we present the results of the multi-wavelength analysis of IRS 13. From the proper motion analysis, we derive the cluster membership of the individual sources. Using photometric measurements in various bands, we classify the observed objects and estimate the related stellar mass. In Figure 3, we show a NACO L-band overview of the region of interest. The region displayed in Figure 3 is called IRS 13 and can be (historically) divided up into IRS 13N and IRS 13E. The north–east nomenclature may result in confusion

Table 2
Mean Dereddened Magnitudes of the DS Analyzed in This Work

ID	H band	K band	L band	K–L	ΔK–L	H–K	ΔH–K
DS1	14.40 ± 0.15	12.37 ± 0.50	10.13 ± 0.33	2.24	0.59	2.03	0.52
DS2	…	…	12.60 ± 0.24	…	…		
DS3	…	…	12.30 ± 0.30	…	…		
DS4	18.27 ± 0.59	15.71 ± 0.35	14.03 ± 1.41	1.68	1.45	2.56	0.68
DS5	…	…	14.37 ± 1.68	…	…		
DS6	18.91 ± 0.2	17.62 ± 0.44	11.43 ± 0.54	6.19	0.69	1.29	0.48
DS7	…	…	11.54 ± 0.48	…	…	…	…
DS8	19.17 ± 0.2	17.57 ± 0.44	12.56 ± 0.76	5.01	0.87	1.60	0.48
DS9	17.11 ± 0.45	14.61 ± 0.76	13.91 ± 1.09	0.7	1.32	2.50	0.88
DS10	16.50 ± 0.31	14.19 ± 0.69	12.82 ± 0.46	1.37	0.82	2.31	0.75
DS11	14.22 ± 0.35	12.10 ± 0.70	10.46 ± 0.64	1.64	0.94	2.12	0.78
DS12	14.04 ± 0.36	11.86 ± 0.72	10.23 ± 0.60	1.63	0.93	2.18	0.80
DS13	18.55 ± 0.46	16.51 ± 0.78	12.80 ± 0.54	3.71	0.94	2.04	0.90
DS14	18.84 ± 0.94	17.33 ± 0.92	12.76 ± 0.39	4.57	0.99	1.51	1.31
DS15	18.77 ± 0.37	17.28 ± 0.53	13.65 ± 0.56	3.73	0.77	1.49	0.64
DS16	18.61 ± 0.71	17.39 ± 1.05	13.75 ± 0.83	3.64	1.33	1.22	1.26
DS17	15.68 ± 0.35	13.28 ± 0.87	11.76 ± 0.64	1.52	1.08	2.40	0.93
DS18	19.75 ± 0.95	17.49 ± 0.40	13.39 ± 0.54	4.10	0.67	2.26	1.03
DS19	19.55 ± 0.01	18.23 ± 0.64	13.95 ± 0.75	4.28	0.98	1.32	0.64
DS20	18.67 ± 0.15	15.81 ± 0.85	13.58 ± 0.72	2.23	1.11	2.86	0.86
DS21	20.23 ± 1.17	17.83 ± 1.01	12.12 ± 0.59	5.71	1.16	2.40	1.54
DS22	19.90 ± 1.21	17.40 ± 0.35	11.91 ± 0.54	5.49	0.65	2.57	1.25
DS23	18.65 ± 0.37	17.33 ± 0.59	14.73 ± 1.39	2.60	1.51	1.32	0.69
DS24	15.07 ± 0.40	13.05 ± 0.74	13.71 ± 1.65	−0.66	1.80	2.02	0.84
DS25	16.28 ± 0.30	14.49 ± 0.75	15.46 ± 1.34	−0.97	1.53	1.79	0.80
DS26	17.20 ± 0.62	15.64 ± 1.16	9.13 ± 0.59	6.51	1.30	1.56	1.31
DS27	14.83 ± 0.29	12.77 ± 0.61	12.08 ± 0.66	0.69	0.89	2.06	0.67
DS28	16.14 ± 0.27	15.80 ± 0.92	10.76 ± 0.42	5.04	1.01	0.34	0.95
DS29	16.17 ± 0.36	14.42 ± 0.86	16.29 ± 1.33	−1.87	1.58	1.75	0.93
DS30	15.67 ± 0.47	13.83 ± 0.74	10.92 ± 0.51	2.91	0.89	1.84	0.87
DS31	14.84 ± 0.29	12.97 ± 1.13	13.08 ± 2.06	−0.11	2.34	1.87	1.16
DS32	16.74 ± 0.32	15.02 ± 0.80	14.71 ± 0.93	0.31	1.22	1.72	0.86
DS33	18.39 ± 1.11	16.16 ± 0.62	9.92 ± 0.57	6.24	0.84	2.23	1.27

Note. We list the mean magnitude (see also Appendix B) and calculate the variance of the individual standard deviation. Hence, the uncertainty of the K–L and H–K colors is given by the square root of the variance and represents the total standard deviation.

because of the proper motion of the IRS 13E–related sources and the coinciding IRS 13N objects. For ease of confusion, we will use the term IRS 13 here only when referring to the sources of IRS 13N and IRS 13E.

3.1. Photometric Analysis

The analysis of about two decades of near-infrared (NIR) and mid-infrared (MIR) NACO data revealed 33 sources that can be observed in various bands in addition to previously known dust-enshrouded objects. In Figure 3, we show the L-band detection of all the investigated sources in this work. In addition, Appendix D and Appendix E reveal the related H- and K-band identification of the dusty sources (DS). The rich data set permits us to produce light curves and individual detections of all new DS objects (Appendix F). Furthermore, Table 2 lists the magnitudes of the newly discovered DS objects. We compare all the known IRS 13 objects with the literature and list the new sources identified in Table 13, Appendix B. Consistent with the literature, we identified all known sources in the L, K, H, and M band. Because every previous analysis of the cluster covered only a fraction of the objects investigated here, our objective was to provide a complete list of all sources with a consistent nomenclature. To avoid confusion with existing studies of the region, we adapt the nomenclature for the brightest sources (E1–E7 and α-ι) of the IRS 13 cluster.

For the analysis of the data, we applied the introduced image sharpener and extracted the positions with a Gaussian fit with dimensions that correspond to the PSF of the data. The FWHM is about 5 to 6 pixels. With a spatial pixel scale for the L-band data of 27 mas, the dimensions of the corresponding PSF are about $1\farcs3$ – $1\farcs6$. For the K-band data and a related spatial pixel scale of 13 mas, the dimensions of the PSF transfer to $0\farcs6$ – $0\farcs7$. Because the sources studied in this work have dominant MIR emissions suffering from reduced confusion and crowding, we focus on the L band and M band whenever the detection of the objects in the NIR is blended. Because of the prominent and variable background of the crowded and dense cluster, we did not apply a local background subtraction, because we consider confusion the dominant source of uncertainty. Especially DS4 and DS5 suffer from confusion and blending effects that are confronted by the usage of the mean covering almost two decades of observations (Table 2).

3.2. Proper motion

Simultaneously with the photometric analysis presented in Section 3.1, we estimate the proper motion of the investigated cluster members. Because of the chance of confusion regarding

Table 3
Proper Motions of the Sources Investigated in This Work Based on *L*-band Observations Carried Out With NACO Between 2002 and 2018

ID	$r_{0,\mathrm{R.A.}}$(mas)	$r_{0,\mathrm{Decl.}}$(mas)	$v_{\mathrm{R.A.}}$(km s^{-1})	$v_{\mathrm{Decl.}}$(km s^{-1})	$\Delta r_{0,\mathrm{R.A.}}$ (mas)	$\Delta r_{0,\mathrm{Decl.}}$(mas)	$\Delta v_{\mathrm{R.A.}}$ (km s^{-1})	$\Delta v_{\mathrm{Decl.}}$(km s^{-1})
α	−2677.0	−1479.1	87.4	51.6	3.2	1.9	18.9	11.5
β	−2890.0	−1246.0	73.4	115.4	3.0	4.1	16.2	21.8
γ	−3088.0	−1003.0	−73.0	170.2	3.4	3.2	18.5	7.8
δ	−2903.6	−854.3	7.9	142.3	1.0	4.3	5.0	26.1
ϵ	−2883.0	−1015.0	42.9	158.9	2.3	6.7	12.9	34.5
ζ	−3150.8	−826.5	−128.9	203.5	5.5	7.7	31.0	42.7
η	−3104.0	−654.9	−27.8	68.0	1.2	2.7	6.6	14.8
ϑ	−2700.0	−892.0	90.4	140.8	4.8	5.5	28.7	32.1
ι	−3043.4	−1240.4	−54.2	81.9	3.4	4.3	18.7	23.8
1	−2795.0	−276.4	−74.0	−94.0	2.0	2.6	13.6	17.1
2	−2954.4	−175.8	9.2	248.0	4.6	10.5	26.4	60.9
3	−3070.9	−251.8	43.5	280.6	4.4	10.1	22.8	57.8
4	−2687.0	−480.3	21.2	−18.8	5.1	2.0	24.6	11.5
5	−2935.5	−408.9	−65.0	117.9	4.6	9.0	30.8	60.3
6	−3182.0	−421.7	−151.6	289.2	6.0	12.8	32.1	62.6
7	−3217.6	−531.3	−124.7	329.7	5.2	11.9	20.2	61.5
8	−3430.4	−636.4	−289.6	443.0	11.7	18.6	67.6	104.6
9	−3597.6	−435.1	31.1	−125.5	3.2	5.6	19.3	35.3
10	−3844.4	−387.9	152.5	−445.1	4.4	10.3	32.3	77.1
11	−2323.4	−891.0	12.3	−56.2	0.9	2.1	4.6	11.3
12	−2484.7	−830.9	175.1	−330.6	5.7	11.4	30.8	62.4
13	−3593.2	−723.4	−381.0	317.9	17.1	14.1	78.8	66.4
14	−3629.7	−867.4	−468.4	242.8	14.3	7.9	74.6	37.9
15	−3526.0	−917.0	−427.7	247.2	20.3	10.4	97.6	47.1
16	−3909.4	−767.9	−17.5	−106.5	3.3	5.5	21.9	33.8
17	−4106.0	−930.8	−61.6	62.1	3.9	2.8	19.6	16.2
18	−4267.0	−858.9	−191.4	−34.7	8.7	5.2	48.9	31.1
19	−4178.5	−956.4	−229.2	−100.4	13.4	7.2	67.2	35.4
20	−4017.9	−1125.5	−190.6	1.7	7.5	2.1	36.6	10.6
21	−3781.6	−1318.7	−327.4	69.3	12.9	2.8	64.7	15.6
22	−3383.1	−1021.1	−187.9	207.5	8.5	9.8	44.0	48.6
23	−2543.5	−1155.7	161.4	5.1	6.8	7.3	39.0	42.2
24	−2461.0	−1441.3	172.1	−93.8	7.8	6.4	38.8	34.1
25	−2410.6	−1687.7	152.6	5.2	5.9	2.6	30.5	13.0
26	−2801.4	−1750.3	103.3	28.9	4.7	2.0	29.5	11.5
27	−3404.0	−720.0	−51.6	−231.9	2.8	7.9	14.7	41.1
28	−2551.8	−1318.4	166.4	124.0	7.6	6.0	43.7	34.0
29	−2429.7	−1719.9	66.85	401.1	8.9	6.6	29.9	22.1
30	−2921.1	−2047.5	66.85	133.7	10.6	7.6	35.6	25.4
31	−2948.4	−1474.2	−200.5	200.5	10.7	5.4	35.6	17.5
32	−2730.0	−1064.7	−468.0	133.7	9.6	4.0	32.2	13.3
33	−2921.1	−1283.1	−200.5	−267.4	10.5	4.5	35.2	15.1
E1	−2935.0	−1637.2	−84.3	−280.0	4.9	10.9	25.4	55.9
E2	−3161.5	−1729.6	−145.2	−86.2	3.8	2.4	24.9	17.3
E3	−3171.0	−1521.0	−71.5	−135.2	3.5	5.4	19.4	27.9
E4	−3201.0	−1424.0	−182.2	23.2	8.4	6.8	38.5	36.7
E5.0	−3401.0	−1528.0	−110.6	45.4	5.2	3.9	31.1	22.0
E5.1	−3413.0	−1579.3	−317.4	−69.6	15.2	8.6	75.1	38.2
E7	−3549.0	−1260.0	148.3	−55.4	6.3	2.5	28.9	12.9

Note. The uncertainties represent the standard deviation. The distance of the DS indicates the related position in 2002.

the detectability of the DS, we use *K*- and *L*-band observations whenever possible carried out with NACO between 2002 and 2019. Except for 2014 and 2015, we trace the objects listed in Table 13 in the majority of available observations. We fit a PSF-sized Gaussian to each individual source to extract its position (Table 3). The origin of our reference frame coincides with the position of Sgr A*. For this, we identify the position of the B2V star S2 and use its well-known and observed orbital solution. From the orbital solution and the position of S2 (Do et al. 2019), we derive the location of Sgr A*. We refer to Appendix C, which lists all positions of S2 and the dusty sources investigated in this work. Because the IRS 13 cluster is about 0.12 pc away from the location of the SMBH, we assume an approximately vanishing velocity $v_{\mathrm{Sgr\,A*}}$ of Sgr A*. Even for objects close to Sgr A*, the velocity effect caused by $v_{\mathrm{Sgr\,A*}}$ is in the subpixel regime (Parsa et al. 2017). We list the resulting proper motion of the DS and all other objects investigated in this work in Table 3. Because of the high degree of crowding, the standard-deviation-based uncertainties may not cover the full set of entities. With upcoming JWST

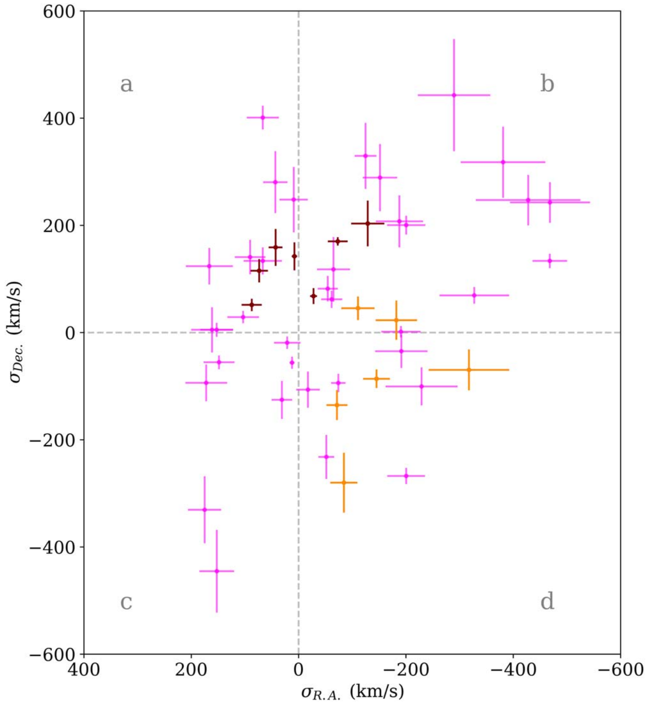

Figure 4. Proper motion of all observed IRS 13 sources (see Figure 3). The E stars (E1–E5) are orange-colored; the brown data points represent the bright dusty sources (α-η). We find a slight over- and underdensity regarding the shown data points in the corresponding quadrant. Please see the text for details.

observations, we expect decreased astrometric uncertainties from the Mid-Infrared Instrument (MIRI) IFU data due to unique Doppler-shifted emission lines. However, we use the results from the presented astrometric analysis to investigate the cluster and the sources for any anisotropy. We will use the approach of Eckart & Genzel (1997) and Genzel et al. (2000), where the authors used the anisotropy parameter to analyze the stellar content of the S cluster. The anisotropy parameter is defined as

$$\gamma_{TR} = \frac{v_T^2 - v_R^2}{v_T^2 + v_R^2} \tag{5}$$

where v_T and v_R refer to the proper motion components perpendicular and parallel to the projected radius vector in the sky, respectively. The anisotropy parameter γ_{TR} provides an accessible numerical approach to investigate IRS 13–related objects for abnormalities. These abnormalities would imply a tendency for a specific stellar type or substructure. A uniform data point distribution indicates a continuous and randomized structure of the cluster. For example, Ali et al. (2020) expected a sine-like distribution for the inclination angle. While this cannot be transferred to the anisotropy parameter, the Gaussian-shaped and uniform cluster discussed in von Fellenberg et al. (2022) can be used for the expected distribution of the dusty sources. Therefore, we will investigate the cluster sample for Gaussian-like structures to investigate the presence of substructures.

In Table 3, we list the resulting proper motions of all investigated objects (Table 13) with the related distances to Sgr A*. Using the proper motions listed in Table 3, we derive the velocity–velocity diagram (Figure 4). From the fit and the

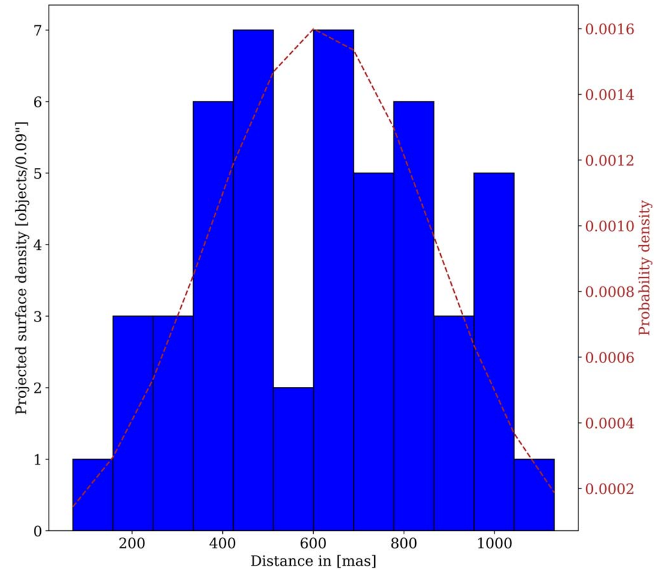

Figure 5. Gaussian distribution of the DS around the geometrical center of IRS 13. The blue-colored histogram shows the number of sources inside the bin of the size of 0.″09. The brown dashed line represents a Gaussian fit of the blue-colored projected surface density. Because the geometrical center of the cluster is in an empty region, the Gaussian probability density drops toward the origin of the stellar distribution.

data points displayed in Figure 4, it is evident that the proper motion of the investigated sources shows an asymmetric distribution around the geometrical center, implying the presence of a trend. Translating this finding to a density as a function of quadrant yields:

1: 13 sources in a (26.5%)
2: 19 sources in b (38.8%)
3: 7 sources in c (14.3%)
4: 10 sources in d (20.4%)

Based on this analysis, the significance of a trend for the proper motion of the DS lacks a reasonable level of explicitness. From the analysis of the proper motion distribution, it is implied that the dusty sources follow a rather uniform arrangement, which is furthermore reflected in the Gaussian-like density probability displayed in Figure 5. This figure shows the Gaussian distribution of the dusty sources around the geometrical center of the cluster as a function of the distance d, which is estimated with $p_{(\mathrm{geo})} = p_{(x,y)} - p_{aver(x,y)}$. In the given relation, $p_{(\mathrm{geo})}$ is the geometrical center of the cluster, $p_{aver(x,y)}$ is the averaged distance of all cluster sources to Sgr A*, and $p_{(x,y)}$ is the averaged distance of a single source between 2002 and 2018. With this, the presentation of the distribution of the DS shown in Figure 5 does not reflect possible existing anomalies of the cluster. Despite the decreased surface density at about 0.″6 indicated in Figure 5, we find a probability density consistent that resembles a Gaussian function as we would expect for a uniform cluster (Genzel et al. 2000). Because $p_{(\mathrm{geo})}$ does not necessarily have to be located at the highest stellar density, the Gaussian fit exhibits an offset from $d = 0$ mas, as illustrated Figure 5. Therefore, we aim to expand the search for substructures and translate the estimated values in Table 3 into the anisotropy parameter γ_{TR} indicated by Equation (5). In the first three plots displayed in Figure 6, we show γ_{TR} as a function of distance from Sgr A* for the E stars, dusty sources, and all combined sources. The apparent continuous distribution

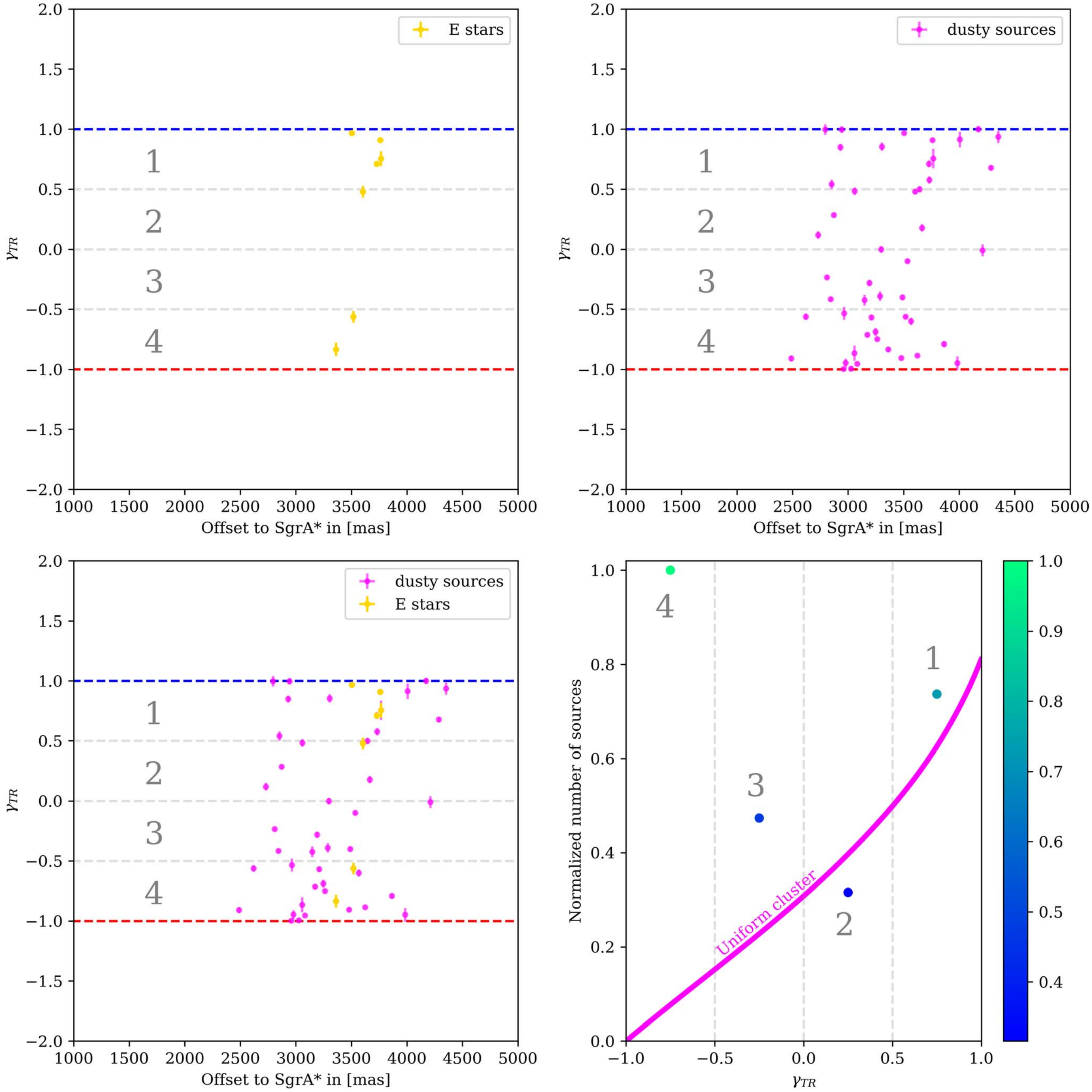

Figure 6. Anisotropy parameter γ_{TR} for the investigated sources in IRS 13. In the upper row, we illustrate γ_{TR} for the E stars (left) and the dusty sources (right). Dividing the anisotropy parameter into four bins reveals an overdensity for some of the sources close to $\gamma_{TR} \approx \pm 1$ implying the existence of substructures. In the lower-left plot, we show all investigated sources of the IRS 13 cluster. The uncertainties of the anisotropy parameters are determined with error propagation of the related standard deviation of the proper motion values (Appendix 3.2). The gray numbers and dashed vertical lines represent the related bin. The lower-right plot shows the normalized number of sources for each bin as a function of γ_{TR}. The magenta-colored line represents the normalized theoretical probability distribution that one would expect for a uniform cluster. The comparison of the observed structure of IRS 13 with a uniform cluster suggests anomalies that are responsible for a nonuniform distribution.

of the data points for all sources illustrated in Figure 4 and Figure 6 is expected because of the shared parameter. However, if we separate the distribution of the anisotropy parameter into four bins with a corresponding size of 0.5 each, we find indications for a slight overdensity close to ± 1. In particular, we find:

1: 14 sources between 1.0 and 0.5
2: 6 sources between 0.5 and 0.0
3: 9 sources between 0.0 and -0.5
4: 19 sources between -0.5 and -1.0

We normalize the distribution to the total number of sources and estimate that about 30% of the sources are in the 0.5 to 1.0 bin, while almost 40% can be found in the -0.5 to -1.0 bin, suggesting an overdensity of sources in bin 1 and bin 4. In particular, this overdensity is reflected in the lower-right plot of Figure 6. There, we show the normalized number of sources as a function of the anisotropy parameter γ_{TR}. In the same plot, we incorporate the theoretical probability distribution (PDF) with a

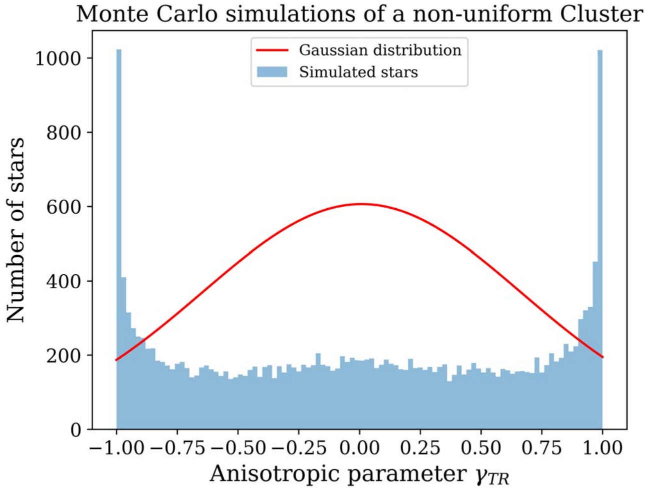

Figure 7. Monte Carlo simulations of γ_{TR} for 10,000 stars. As we have shown in Figure 6, the anisotropy parameter peaks at ±1, which indicates a nonuniform cluster. In comparison, we show a Gaussian distribution.

constant anisotropy, where we adapt the corresponding normalized function

$$\mathrm{PDF}(\gamma_{TR})\mathrm{d}\gamma_{TR} = \frac{\mathrm{n}!(\sqrt{1+\gamma_{TR}})^{2n-1}}{\pi(2\mathrm{n}-1)!!\sqrt{1-\gamma_{TR}}}\mathrm{d}\gamma_{TR} \tag{6}$$

from Genzel et al. (2000). In the above equation, n refers to a power-law distribution index with $\beta = 1/2 - n$. We can now assume numerical values representing a constant anisotropy that classifies uniform clusters. For example, the magenta PDF in the lower-right plot of Figure 6 is calculated with Equation (6) and a constant anisotropy of $\beta = -3/2$ resembling the results of Genzel et al. (2000).[8] From the data points representing the sources in IRS 13 shown in Figure 6, it becomes directly obvious that the cluster is not uniform and shows anisotropy that peaks at ±1 in strong agreement with Genzel et al. (2000). However, for the results displayed in Figure 6, we picked only one numerical value for β to maintain clarity. To inspect the expected distribution of an anisotropic cluster, we use Monte Carlo simulations, shown in Figure 7. This figure strengthens our results, which show a peak of γ_{TR} at ±1 as well. In Figure 7, we simulate 10,000 stars and find an overdensity at $\gamma_{TR} \pm 1$ as for IRS 13. Therefore, the investigated cluster that harbors the dusty sources is not uniform. In addition, we estimate a velocity dispersion from the data listed in Table 3 and illustrated in Figure 4 of 128.86 ± 0.14 km s^{-1} for the cluster. From this we can directly derive the mass that is needed to bind the stars to the cluster. With $M_{\mathrm{IRS13}} = \langle v^2 \rangle \cdot R/G$ where $R = 0.01$pc donates the approximate size of the cluster and G the gravitational constant, we get $\sim(3.9 \pm 0.1) \times 10^4 M_\odot$ in agreement with independently calculated literature values (see Schödel et al. 2005; Paumard et al. 2006; Tsuboi et al. 2017b, 2020b). This enclosed mass estimate can be used to calculate the Hill radius r_{Hill} to inspect the gravitational bounds of the IRS 13 cluster.

[8] Please refer to Figure 9 in Genzel et al. (2000).

Table 4
Dereddened Reference Values for IRS 2L Used in This Work Based on the Analysis of Viehmann et al. (2006)

Filter	Magnitude [mag]	Flux$_\lambda$ (Jy)	A_X
H band	14.26	0.13	4.37
K band	10.60	0.48	2.80
L band	6.4	2.98	1.45
M band	5.5	3.98	0.58

Note. The reddening vector A_X for the corresponding band is adapted from Viehmann (2007) assuming an optical extinction of $A_V = 25$m ag (Scoville et al. 2003) using the extinction law from Rieke & Lebofsky (1985). We refer to Fritz et al. (2011) for a detailed discussion of the optical extinction A_V.

We use

$$r_{\mathrm{Hill}} = D(M_{\mathrm{IRS13}}/3M_{\mathrm{SgrA*}})^{1/3}, \tag{7}$$

where D donates the distance to Sgr A* and $M_{\mathrm{SgrA*}}$ the related mass of the SMBH. We use $D = 0.15$ pc and $M_{\mathrm{SgrA*}} = 4 \times 10^6 M_\odot$ (Peißker et al. 2022; Event Horizon Telescope Collaboration et al. 2022) and get $r_{\mathrm{Hill}} = 0.022\,pc = 22$ m pc. Because we investigate the complete IRS 13 region, including the E stars and the dusty objects (Figure 3), r_{Hill} is in remarkable agreement with the measured diameter of the cluster core region (≈45m pc, see Section 4).

3.3. Photometric Analysis

We use a multiwavelength approach to investigate the nature of the brightest *M*-band dust objects in the IRS 13 cluster (Figure 8). Starting from Figure 8 in the *M* band, we analyze the emission of the dust objects in the *H*, *K*, and *L* band (see also Figure 3). Because Viehmann et al. (2006) analyzed an extensive amount of stellar sources in the environment of Sgr A* in various bands (see also Bhat et al. 2022), we use the close-by star IRS 2L as a reference source (Table 4). Because Viehmann et al. used part of the here investigated data set, the choice of the reference star ensures a consistent photometric approach. Because of the dominant contribution of Wolf-Rayet and O stars E1, E2, E3, and E4 (Maillard et al. 2004) in all the bands, we will use a high-pass filter to minimize the PSF wings. This process used is already described in detail in Section 2.4 and Peißker et al. (2022). The photometric robustness of high-pass filters compared with the raw data is further investigated in Ott et al. (1999). To inspect the validity of the proposed photometric robustness discussed in Ott et al., we compare the estimated *L*-band magnitudes of DS1 (Figure 3) in the raw data with the results of the high-pass filtering. As listed in Table 5, we do not find a significant difference between the filtered and nonfiltered data in agreement with the analysis of Ott et al. (1999). We would like to emphasize that the analysis of the investigated dusty objects focuses on the colors defined as the difference between two magnitudes. The colors are not affected by systematic differences potentially induced by the applied high-pass filter, because variations would be canceled out. However, using Equation (1) with the magnitudes of reference star IRS 2L (Table 4), we estimate the magnitudes for the dusty sources and the main-sequence stars E1–E7 (Figure 8). Consult Table 6 for the related values, including the standard deviation. From the *H*–*K* and *K*–*L* colors of the investigated sources, we do find a substantial difference between the two groups (dusty sources—

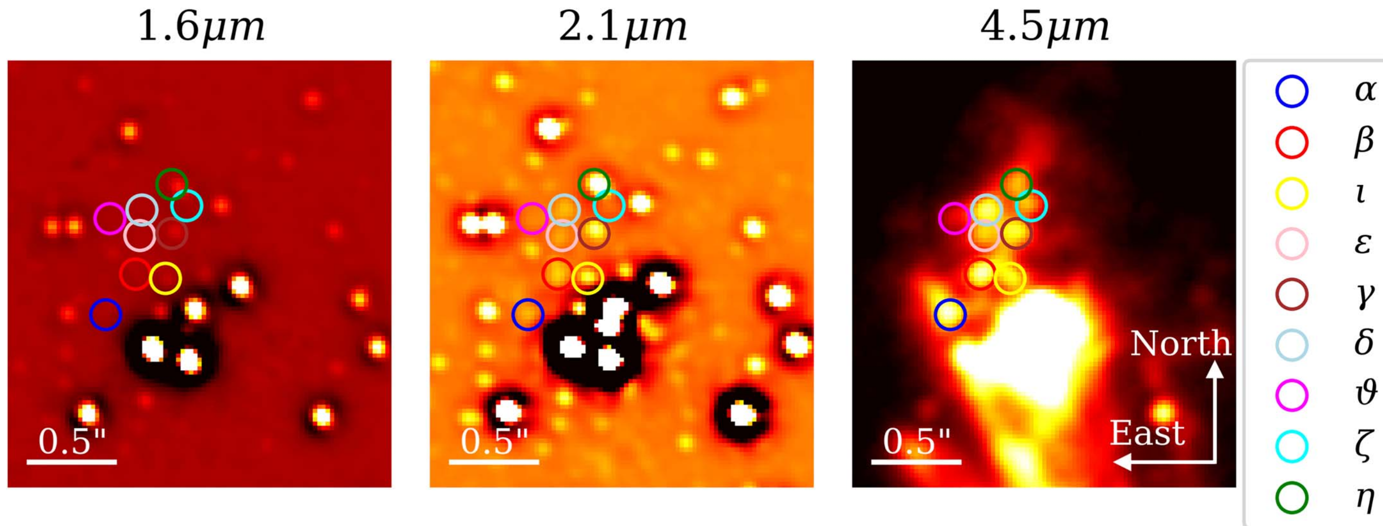

Figure 8. Multiwavelength view toward IRS 13 observed with NACO. To minimize the influence of dominating PSF wings, we apply an image sharpener to the *H* and *K* band observed at 1.6 μm and 2.1 μm, respectively. The prominent dust features are revealed in the MIR (here: 4.5μm) and are not treated with any filter. Every image was normalized to its peak emission flux. The contrast was adjusted to visualize the presence of the dusty sources in the related band. However, the lower cutoff resulted in regions around bright stars with apparent missing flux. We note that sources such as E3 close to E4 (see Figure 3) have an *H*-band emission but are suppressed because of the contrast settings.

E stars) of cluster members (Figure 9). In addition to the sources investigated here, we also include magnitudes from the related publication of various other objects, such as DSO/G2 (Peißker et al. 2021c), X3 (Peißker et al. 2023b), and X7 (Peißker et al. 2021a). A complete list of all used sources analyzed for Figure 9 is listed in Table 6. The findings presented in Figure 9 agree with the studies and classifications presented in Peißker et al. (2020c) and will be discussed in Section 4. Because we derived the magnitudes of the IRS 13 sources, we will estimate the related flux density and the corresponding uncertainties with Equation (2). The flux density is useful to estimate the spectral energy distribution (SED) of the individual sources, which will be presented in the next section. Compared with the literature, we maximize the spectral coverage and include the radio data observed[9] with ALMA (Figure 10) and previously analyzed, e.g., in Tsuboi et al. (2017b). Because of the science-ready character of the calibrated data, we list the corresponding flux values of the dusty sources in Table 7.

3.4. Spectral Energy Distribution

The spectral analysis of the O- and W-type stars of the IRS 13 cluster is well covered in the literature (Maillard et al. 2004). Despite bright emission in various bands, the dusty sources analyzed in the literature lack a detailed spectral analysis. We apply the 3D radiative transfer model implemented in the HYPERION code and incorporate the results listed in Table 6 and Table 7. These flux density values are used as input parameters from which HYPERION estimates the best-fit SED. The spectrum is renormalized and ensures a high synergy between the observations and the simulations. The uncertainties of the input flux density values (Table 6) estimated from the standard deviation do account for a variable background, close-by sources, and the stellar density as well as the embedded structure (eminent in the *L* and *M* band) of the cluster.

[9] PI: Masato Tsuboi

Table 5
Photometric Comparison of the Applied Analysis Tools for DS1 in the *L* band

Year	No filter	Filter	Mean	Δ Mean
2002	10.75	10.95	10.85	± 0.10
2003	10.70	10.85	10.77	± 0.07
2004	10.46	10.75	10.60	± 0.15
2005	10.50	10.68	10.59	± 0.09
2006	10.40	10.64	10.52	± 0.11
2007	10.27	10.36	10.31	± 0.04
2008	10.05	10.32	10.18	± 0.13
2009	10.13	10.34	10.23	± 0.10
2010	10.12	10.25	10.18	± 0.06
2011	9.88	10.09	9.98	± 0.10
2012	9.98	10.03	10.00	± 0.02
2013	10.09	10.21	10.15	± 0.06
2014	…	…	…	…
2015	…	…	…	…
2016	9.42	9.58	9.50	± 0.08
2017	9.88	10.19	10.03	± 0.15
2018	10.31	10.27	10.29	± 0.02
Average	10.19	10.36	10.27	0.08
Median	10.13	10.32	10.27	0.08

Note. For the mean, we average the magnitude derived from the high-pass-filtered and nonfiltered data. The magnitude differences are marginal and smaller than the usual standard deviation as presented in Table 2.

To motivate the usage of HYPERION, which models the emission of YSOs, we refer to the color–color diagram shown in Figure 9, which justifies our approach. Incorporating the derived flux and uncertainty values, we find a best-fit solution for the spectral energy distribution of the dusty sources, as shown in Figure 11. We list related input parameters, such as stellar mass and luminosity, in Table 8. In agreement with the top-heavy mass function derived by Paumard et al. (2006) and Lu et al. (2013), we find several massive and high-mass YSOs in the IRS 13 cluster, in line with its exceptional high core density of $\rho_{\rm core} \geqslant 3 \times 10^8 M_\odot$ pc^{-3} (Paumard et al. 2006). Except for η, all investigated sources exhibit a stellar mass between 4.0 and 10.0 $M_\odot$. Taking into account the stellar

Table 6
Dereddened Magnitude and Flux Estimates of the E Stars and the Brightest Dusty Sources of the IRS 13 Cluster (See Figure 3)

ID	*H* Band		*K* Band		*L* Band		*M* Band		*K–L*	*H–K*
	(mag)	(mJy)	(mag)	(mJy)	(mag)	(Jy)	(mag)	(Jy)		
α	20.68 ± 0.85	$0.35^{+0.41}_{-0.19}$	15.75 ± 0.14	$4.18^{+0.57}_{-0.50}$	9.48 ± 0.30	$0.17^{+0.05}_{-0.04}$	7.56 ± 0.17	$0.59^{+0.10}_{-0.08}$	6.27 ± 0.29	4.93 ± 0.29
β	19.74 ± 0.04	$0.83^{+0.03}_{-0.03}$	15.18 ± 0.21	$7.06^{+1.50}_{-1.24}$	8.79 ± 0.78	$0.32^{+0.34}_{-0.16}$	7.57 ± 0.14	$0.59^{+0.08}_{-0.07}$	6.39 ± 0.29	4.56 ± 0.13
γ	16.28 ± 0.20	$20.22^{+4.09}_{-3.40}$	14.19 ± 0.30	$17.58^{+5.59}_{-4.24}$	9.26 ± 0.98	$0.21^{+0.31}_{-0.12}$	7.91 ± 0.29	$0.43^{+0.13}_{-0.10}$	4.93 ± 0.34	2.09 ± 0.05
δ	19.56 ± 0.48	$0.98^{+0.54}_{-0.35}$	15.90 ± 0.28	$3.64^{+1.07}_{-0.82}$	9.16 ± 0.76	$0.23^{+0.23}_{-0.11}$	7.70 ± 0.17	$0.52^{+0.08}_{-0.07}$	6.74 ± 0.09	3.66 ± 0.52
ϵ	…	…	16.27 ± 0.22	$2.58^{+0.58}_{-0.47}$	9.50 ± 1.16	$0.17^{+0.32}_{-0.11}$	8.34 ± 0.52	$0.29^{+0.17}_{-0.11}$	6.77 ± 0.69	…
ζ	20.06 ± 0.46	$0.62^{+0.32}_{-0.21}$	16.01 ± 0.62	$3.29^{+2.53}_{-1.43}$	9.38 ± 0.84	$0.19^{+0.22}_{-0.10}$	8.12 ± 0.29	$0.35^{+0.10}_{-0.08}$	6.63 ± 0.11	4.05 ± 0.09
η	15.29 ± 0.16	$50.34^{+7.99}_{-6.89}$	12.80 ± 0.19	$63.27^{+12.10}_{-10.15}$	9.25 ± 0.71	$0.21^{+0.19}_{-0.10}$	8.11 ± 0.23	$0.35^{+0.08}_{-0.06}$	3.55 ± 0.26	2.49 ± 0.02
ϑ	21.04 ± 0.25	$0.25^{+0.06}_{-0.05}$	…	…	10.29 ± 1.22	$0.08^{+0.17}_{-0.05}$	9.14 ± 0.39	$0.13^{+0.06}_{-0.04}$	…	…
ι	16.67 ± 0.21	$14.12^{+3.01}_{-2.48}$	14.23 ± 0.29	$16.95^{+5.19}_{-3.97}$	9.71 ± 1.62	$0.14^{+0.48}_{-0.10}$	8.12 ± 0.45	$0.35^{+0.18}_{-0.12}$	4.52 ± 0.66	2.44 ± 0.25
	(mag)	(Jy)	(mag)	(Jy)	(mag)	(Jy)	(mag)	(Jy)		
E1	11.16 ± 0.06	$2.25^{+0.12}_{-0.12}$	9.19 ± 0.17	$1.75^{+0.29}_{-0.25}$	7.69 ± 0.65	$0.90^{+0.74}_{-0.40}$	6.96 ± 0.33	$1.03^{+0.36}_{-0.27}$	1.50 ± 0.23	1.97 ± 0.03
E2	11.31 ± 0.08	$1.96^{+0.15}_{-0.13}$	9.23 ± 0.21	$1.69^{+0.36}_{-0.29}$	7.07 ± 0.64	$1.60^{+1.29}_{-0.71}$	6.17 ± 0.27	$2.14^{+0.60}_{-0.47}$	2.16 ± 0.21	2.08 ± 0.02
E3	14.43 ± 0.59	$0.11^{+0.08}_{-0.04}$	10.79 ± 0.67	$2.66^{+0.34}_{-0.18}$	6.52 ± 0.51	$2.66^{+1.59}_{-1.00}$	5.17 ± 0.01	$5.39^{+0.04}_{-0.04}$	4.27 ± 0.08	3.64 ± 0.26
E4	12.62 ± 0.15	$0.58^{+0.08}_{-0.07}$	10.25 ± 0.33	$1.45^{+0.23}_{-0.17}$	7.18 ± 0.65	$1.45^{+1.19}_{-0.65}$	6.15 ± 0.15	$2.18^{+0.32}_{-0.28}$	2.77 ± 0.31	2.37 ± 0.08
E5.0	…	…	14.24 ± 0.41	$0.65^{+0.01}_{-0.01}$	8.04 ± 0.99	$0.65^{+0.97}_{-0.39}$	6.68 ± 0.31	$1.34^{+0.44}_{-0.33}$	6.20 ± 0.70	…
E5.1	…	…	14.53 ± 0.09	$0.61^{+0.01}_{-0.01}$	8.11 ± 0.87	$0.61^{+0.75}_{-0.34}$	6.95 ± 0.29	$1.04^{+0.32}_{-0.24}$	6.42 ± 0.48	…
E7	13.21 ± 0.11	$0.54^{+0.02}_{-0.02}$	10.61 ± 0.11	$0.32^{+0.05}_{-0.04}$	8.82 ± 0.71	$0.32^{+0.29}_{-0.15}$	8.92 ± 0.85	$0.17^{+0.20}_{-0.09}$	1.79 ± 0.29	2.60 ± 0.05
	(mag)	(Jy)	(mag)	(Jy)	(mag)	(Jy)	(mag)	(Jy)		
IRS 3	14.68 ± 0.12	$0.08^{+0.02}_{-0.01}$	9.66 ± 0.62	$1.14^{+0.88}_{-0.49}$	6.03 ± 0.03	$4.19^{+0.11}_{-0.12}$	2.99 ± 0.14	$40.16^{+5.53}_{-4.86}$	3.63 ± 0.32	5.02 ± 0.35
IRS7	9.26 ± 0.04	$13.12^{+0.36}_{-0.60}$	6.50 ± 0.10	$20.95^{+2.02}_{-1.85}$	6.01 ± 0.05	$4.26^{+0.20}_{-0.19}$	3.12 ± 0.49	$35.63^{+20.33}_{-11.94}$	0.49 ± 0.08	2.76 ± 0.07

Note. For comparison, we also list the measured values of IRS 3 and IRS 7. The indicated uncertainties of the magnitudes and fluxes for all objects are based on the standard deviation except for IRS 3 and IRS 7. The uncertainties for the two bright stars are adapted from published studies, namely Blum et al. (1996), Viehmann et al. (2006), and Pott et al. (2008). The used reference magnitudes for IRS 2L are listed in Table 4. For ϵ, E5.0, and E5.1, we do not find *H*-band emission above the detection limit, which might be due to confusion. The uncertainties of the magnitudes and fluxes reflect the standard deviation. As pointed out by Fritz et al. (2010) and implied by the east–west elongation indicated in Eckart et al. (2004), E3 may be a collection of several less luminous stars. Controversially, Tsuboi et al. (2017b) associates E3 with the location of a possible IMBH.

properties of the dusty sources in combination with the accretion rate (denoted as the infall rate in Table 8), we classify these objects as massive Herbig Ae/Be stars. Because of their nature, these dusty sources have an age of 10^4–10^5 yr and show a strong photometric correlation (Figure 9) with the recent discovery of the HMYSO X3 (Peißker et al. 2023b). Regarding η, more data are needed to classify the low-mass source. However, the shape of the related SED implies that η could be associated with a low-mass T Tauri star (Beckwith et al. 1990; Kenyon & Hartmann 1995).

4. Discussion

In this section, we will discuss the results presented above. We will introduce a new substructure of the IRS 13 cluster and motivate detailed upcoming observations in the mid-infrared. Taking into account the results presented, we will further suggest expanding the existing view toward the dimension of the IRS 13 cluster. It is suggested that the cluster shows an elongated tail that is caused by the gravitational interaction of Sgr A* with IRS 13.

4.1. Stellar Content of the System

NACO *L*-band observations of IRS 13 revealed 33 unknown objects in addition to previously investigated dust and stellar sources (Table 13; see Maillard et al. 2004; Eckart et al. 2013). The brightest sources, donates with Greek letters, can be observed in various bands ranging from the infrared to the radio/submm domain. Because the majority of the studied MIR dust sources exhibit *K*- and *H*-band NIR counterparts (see Appendix D and Appendix E), a stellar nature is inevitable. Compared with the main-sequence E stars (O/WR-type), the *K–L* and *H–K* colors of the dusty sources are represented by two to three times higher numerical values. These high-infrared *H–K* and *K–L* colors suggest, together with the survey of Ishii et al. (1998), a YSO classification for the bright dusty objects of IRS 13. Further studies of YSOs were carried out by Lada & Adams (1992), who used *J–H* and *H–K* colors for their classification. Although the geometrical composition of the circumstellar components influences the NIR emission of YSOs, our derived *H–K* colors are in agreement with studies of intermediate and high-mass YSOs (see also Berrilli et al. 1992). A further indicator that underlines the classification of the dusty sources as YSOs is illustrated in Figure 11. The flux density values, covering a spectral range between the IR and the submm/radio, are fitted with a model representing the typical emission of Class I YSOs. While the best-fit models presented in Figure 11 do not necessarily exclude other interpretations of the flux density distribution of the dusty sources, it is still a strong footprint of YSOs. Observations with the JWST and MIRI will potentially reveal typical emission lines that are associated with YSOs (see Section 4.6). We note that there is increased confusion and noise level when investigating *J*-band NACO observations, which requires a detailed data-processing method such as the Lucy Richardson deconvolution algorithm (Lucy 1974). However, these analysis steps exceed the scope of this work and will be part of a future publication. It should be

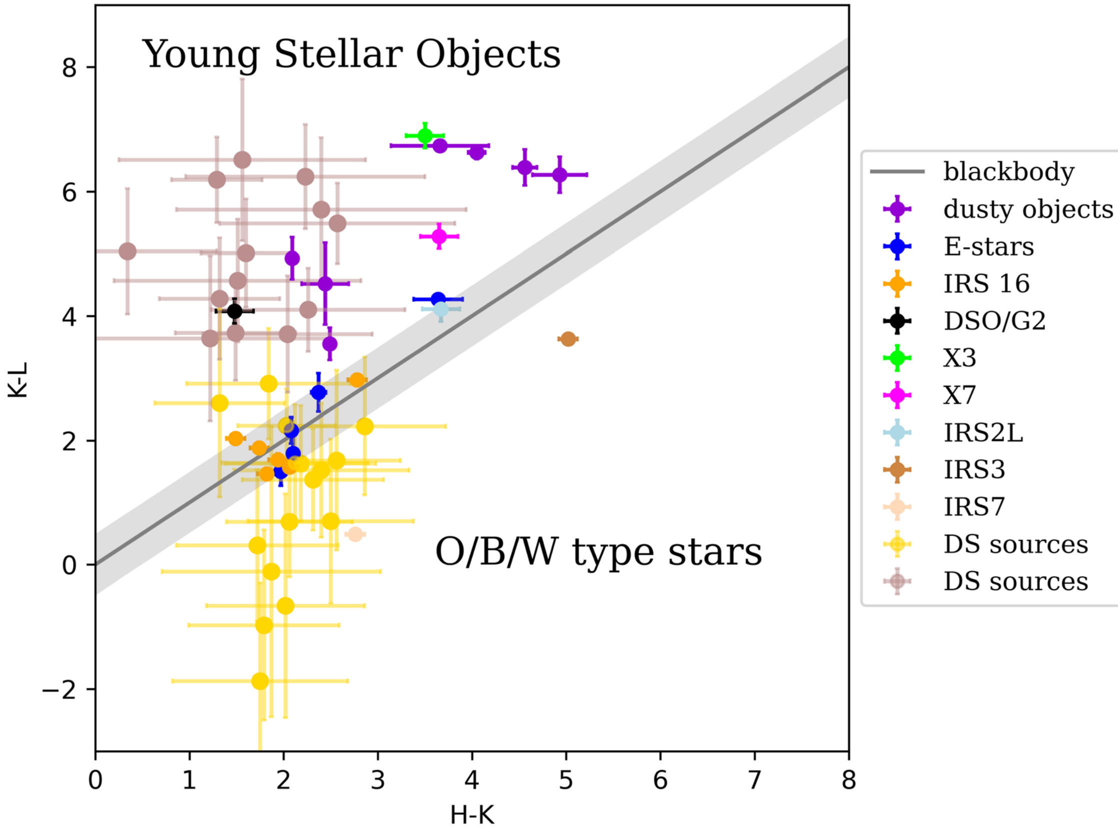

Figure 9. Color–color diagram for some prominent stellar objects in the *inner parsec*. The linear gray line represents a one-component blackbody with increasing temperature and separates known evolved and embedded early-type stars from candidate YSOs (see also Ishii et al. 1998; Eckart et al. 2004). Based on this classification, the photometric data imply two generations of dusty sources, namely YSOs (brown) and main-sequence stars (yellow). Please note that the photometric uncertainty of two DS, DS23 and DS30, forbids a strong statement about their exact nature. Overall, the uncertainties represent the standard deviation of the estimated colors listed in Table 6. Here, IRS 16 refers to the stars indicated in Figure 3.

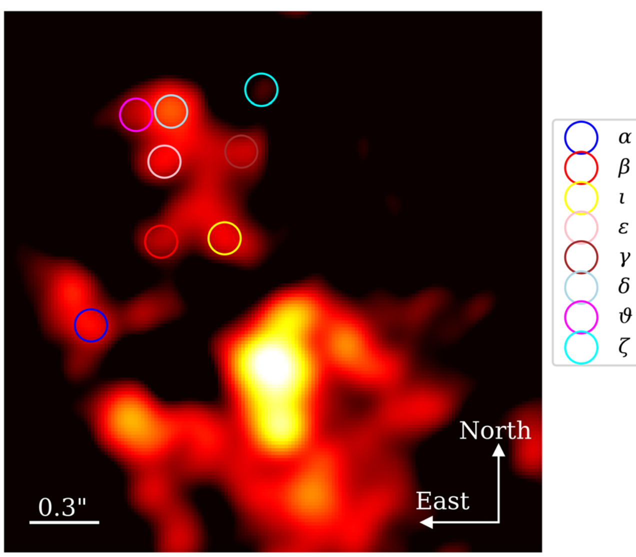

Figure 10. Observation of the IRS 13 cluster with ALMA. The data were observed at 343 GHz and correspond to CO ($v = 0$). The location of the bright dusty sources that are observed in the infrared is indicated by colored circles. Like the E stars, the projected location of the dusty sources implies clustering. The related flux of the individual sources in listed in Table 7.

noted that the classification of the brightest L-band sources in our sample exhibits a flux density distribution that agrees very well with class I YSOs except for η. The SED of this source shows similarities to a low-mass T Tauri star (Chiang & Goldreich 1997; Scoville & Burkert 2013). Hence, we will focus on the rather ambiguous classification of η using the J–H and H–K colors. Despite the challenges with respect to the J-band analysis of the dusty sources of IRS 13, we identify η without confusion about noise (Figure 12), and infer a related

Table 7
Flux Density Values for the Dusty Objects Derived From CO ALMA Observations

ID	CO (v=0), 343 GHz [mJy]
α	1.43 ± 0.5
β	1.05 ± 0.5
γ	1.09 ± 0.5
δ	1.91 ± 0.5
ϵ	1.38 ± 0.5
ζ	0.61 ± 0.5
η	$(0.19 \pm 0.5)^{*}$
ϑ	$(1.15 \pm 0.5)^{**}$
ι	1.29 ± 0.5
IRS 3	129.1 ± 55.1
IRS7	34.4 ± 0.4

Note. Please see Figure 10 for the related source identification. For η, we only estimate an upper limit, whereas ϑ seems to be confused with δ. We use IRS 13E3 as a reference source with a corresponding peak flux of 10.5 ± 0.5 mJy and adapt the uncertainty as proposed in Tsuboi et al. (2017a). These submm/radio flux values in combination with the IR values listed in Table 6 are used for the input spectrum of HYPERION.

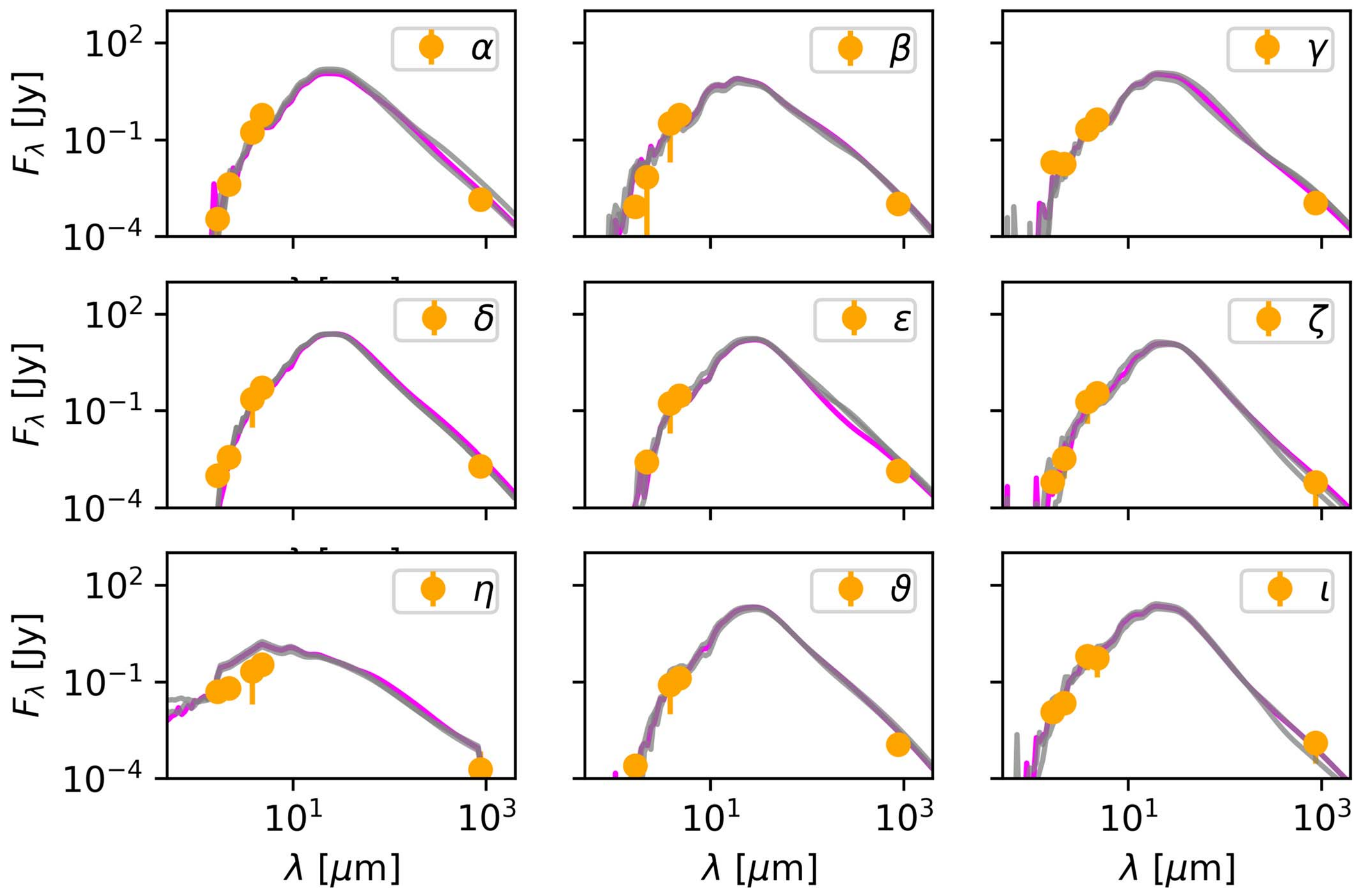

Figure 11. Best-fit SED of the brightest dusty sources in the IRS 13 cluster representing the YSO parameters given in Table 8. The input spectrum is constructed using the flux density values listed in Tables 6 and 7. The associated numerical flux density values, including their related uncertainty, are implemented in the SED plots to emphasize the validity of the resulting best-fit parameters. For almost every source, the solution in magenta represents the best fit and is associated with an inclination of about 90°, while the gray SED is related to the maximum and minimum uncertainty indicated in Table 8. The inclination for the SED, including the related uncertainties of the source η, equals 70°.

Table 8
Best-fit Parameters Describing the Flux Density Distribution of the Dusty Sources of IRS 13 Indicating Their Stellar Nature Using the Radiative Transfer Model HYPERION

ID	Mass ($M_\odot$)	Luminosity ($10^3 \times L_\odot$)	Infall rate ($10^{-6} \times \dot{M}_\odot$)	Radius ($R_\odot$)	Disk mass ($M_\odot$)	Disk size (AU)	Envelope size (AU)
α	5.0 ± 1.0	9 ± 1	5 ± 1	2 ± 0.5	0.1 ± 0.01	0.06-200	0.09-500
β	8.0 ± 1.0	10 ±	0.3 ± 1	3 ± 0.5	0.01 ± 0.005	0.04-200	0.09-350
γ	6.0 ± 1.0	9 ± 1	0.3 ± 0.1	4 ± 1	0.05 ± 0.01	0.04-200	0.09-500
δ	10.0 ± 2.0	11 ± 1	0.5 ± 0.1	3 ± 1	0.01 ± 0.001	0.04-200	0.09-700
ϵ	7.0 ± 2.0	7 ± 2	0.5 ± 0.1	3 ± 2	0.1 ± 0.01	0.04-200	0.09-700
ζ	4.0 ± 1.0	7 ± 1	0.3 ± 0.1	3 ± 1	0.06 ± 0.01	0.04-100	0.09-500
η	0.5 ± 0.2	2 ± 0.5	…	0.8 ± 0.2	0.005 ± 0.002	0.13-50	…
ϑ	7.0 ± 1.5	8 ± 1	0.5 ± 0.1	3 ± 1	0.01 ± 0.02	0.04-200	0.04-700
ι	10 ± 2.0	12 ± 2	0.05 ± 0.01	7 ± 2	0.5 ± 0.1	0.02-100	0.04-700

Note. We motivate the application of the radiative transfer model describing YSOs by the clear color–color classification shown in Figure 9. Considering the pronounced slope of the NIR/MIR SED and their related position in the color–color diagram, it is suggested that the nature of these sources allows the classification as candidate YSOs (class I) (Lada 1987). For a demonstration of HYPERION's feedback after incorporating the estimated flux density values for IRS 3, please refer to Section 4.2.

magnitude of $\mathrm{mag}_J = 18.8 \pm 0.6$ that results in $J–H = 3.5$ with $H–K = 2.5$ (Table 6). Taking into account the color–color analysis of Lada & Adams (1992), Ito et al. (2008), and Ojha et al. (2009), η appears to be a low-mass class I YSO that conflicts with the results of the radiative transfer model presented in Section 3.4 because of the missing envelope.

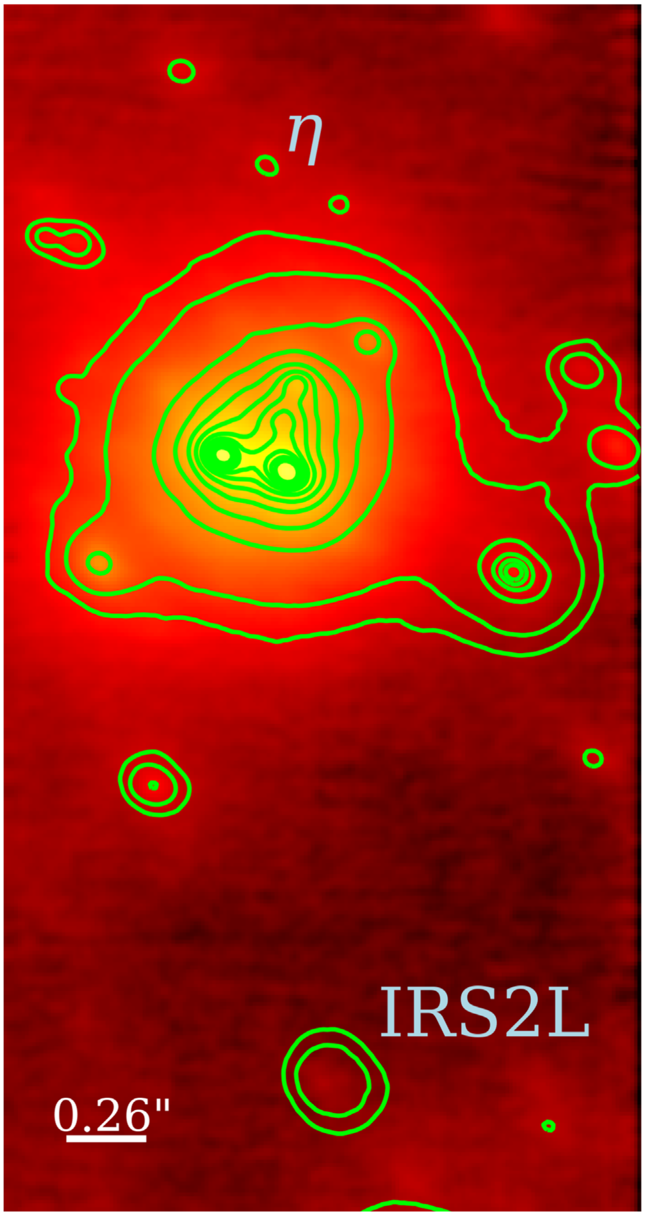

Figure 12. *J*-band observation of IRS 13 with NACO in 2013. We overlaid lime-colored contour lines adopted from the *K*-band observations of the same epoch and instrument. The contour levels represent 0.75%, 1%, 2%, 3%, 4%, 5%, 6%, 7%, 8%, 9%, and 10% of the normalized *K*-band NACO data. The faint emission of IRS 2L is labeled at the corresponding *K*- and *L*-band position, whereas the bright emission is associated with IRS 13. We further indicate the position of the low-mass class I YSO η. Here, north is up, and east is to the left.

We can only speculate on possible explanations for the interplay of the missing envelope with the photometric footprint of a class I YSO candidate. One option could be the intrinsic orientation of the system toward the observer. As implied by the SED results present in Figure 11, the inclination does have a considerably large impact on the shape of the distribution. Another option could be an evolutionary transition to the class II stage or a partial detachment of the envelope, as is already suggested for the class I YSO L1489 IRS (Brinch et al. 2007). Despite the exact classification, the global interpretation as a low-mass YSO is still plausible. Because DSO/G2 (Peißker et al. 2021c) is also classified as a low-mass YSO (see Zajaček et al. 2017), it is implied that both sources share a common nature. In summary, the general trend suggests that sources above the solid line illustrated in Figure 9 can be classified as YSOs, which implies that IRS 13 harbors two generations of stellar objects.

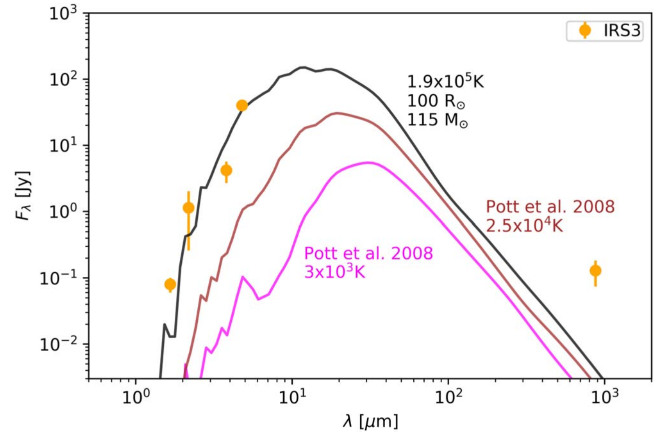

Figure 13. Comparison of different input parameters for the flux density values (orange-colored dots) estimated for IRS 3 (Table 6). Please note that the magenta- and brown-colored SED is based on the stellar parameters derived by the interferometric broadband analysis by Pott et al. (2008). Assuming a hypothetical YSO association with IRS 3 results in unsatisfying outcomes of the radiative transfer model fit. Only a speculative stellar temperature of $1.9 \times 10^5 K$ seems to reproduce the NIR and MIR flux. The submm/radio emission is not fitted by any of the presented SED solutions. Please see the text for details.

4.2. Validity of the Radiative Transfer Model

Here we want to take a critical look at the results regarding the classification of the dusty sources as YSOs. In Eckart et al. (2004), the authors proposed for the first time the idea of associating the dusty sources of IRS 13 using a color–color diagram such as the one displayed in Figure 9. In agreement with Eckart et al. (2004) and the analysis of X3 presented in Peißker et al. (2023b), we found distinguishing colors compared with known main-sequence stars such as IRS 3 (Pott et al. 2008). To expand the color–color analysis of the dusty sources, we decided to apply the radiative transfer code HYPERION (Robitaille 2011, 2017) to the flux density values listed in Table 6. Although we find satisfying solutions to the flux density values in combination with the colors of the dusty sources (Figure 11), the outcome of the radiative transfer model could be biased because we already assumed a YSO classification. Therefore, we want to investigate the validity of this approach by using the class I model used for the SED shown in Figure 11 with the flux density values of the embedded and cool carbon star IRS 3. This star is most probably in the helium-core burning phase with a related stellar temperature of 3000 K based on the interferometric observations carried out with the MID-infrared Interferometric instrument/Very Large Telescope Interferometer (Leinert et al. 2003; Pott et al. 2008). For the stellar analysis of IRS 3 presented in Pott el al., the authors used the 1D radiative transfer code DUSTY (Ivezic et al. 1999), which is developed for AGB stars exhibiting radiatively driven winds. The NIR and MIR flux density values for IRS 3 listed in Table 6 are in reasonable agreement with the results presented in Figure 16 in Pott et al. (2008). Deviations between our estimated flux values and the ones derived by Pott et al. are reflected by the uncertainties given in Table 6 and the error bars shown in

Table 9
Generation of Stars Inside the IRS 13 Cluster With Their Related Origin and Current Location

	1. Generation	2. Generation
Approx. age [Myr]	4	<1
Birthplace	CND	Bow-shock shell
Current location inside IRS 13	Core	Tip
Mean *K*–*L* index	2.49	5.72

Note. In addition, we list the mean *K*–*L* color of the sources listed in Table 6. We exclude E5.0 and E5.1 from the mean colors because of their missing *H*-band counterpart, which may be related to confusion or their nature. The majority of the sources considered in this list can be categorized as high-mass objects. See Figure 14 for the location of the sources.

Figure 13. Using the estimated stellar properties of Pott et al. (2008) results in the magenta-colored SED displayed in Figure 13. Comparing the magenta-colored result with the measured flux density of IRS 3 reveals that HYPERION is not suitable to reflect the SED of the star. Using the upper limit of Pott el al. for a hot C-rich star with an amorphous carbon grain-dominated circumstellar dust distribution produces the brown-colored SED shown in Figure 13. In summary, the authors of Pott et al. conclude that IRS 3 is a cool carbon AGB star. However, we speculatively implement a stellar temperature of $1.9 \times 10^5 K$ in our radiative transfer model and find that this setting reflects the NIR and MIR emission. Neither of the presented SED solutions for IRS 3 using HYPERION fits the submm/radio flux. Taking into account the silicate absorption feature of IRS 3 observed in the *N* band (Pott et al. 2008), we can safely conclude that our speculative solution (black SED, Figure 13) is not valid. It is further well known that the existence of silicates requires a stellar temperature of a few 1000 K (Kozasa & Sogawa 1999; Tsuchikawa et al. 2021), in line with the established results for IRS 3 in the literature. Therefore, we conclude that the SED solution displayed in Figure 11 is a strong indication for the classification of the dusty sources as YSOs. The radiative transfer model HYPERION is not suitable for embedded main-sequence stars, which emphasize the color–color results presented in Figure 9.

4.3. Formation Scenarios for the IRS 13 Cluster

Because of the complexity of possible formation scenarios for the IRS 13 cluster, we refer to Paper II. However, we briefly want to outline the basic idea to explain the findings presented in this work. As proposed by Wang et al. (2020),[10] the resulting trajectory of the young cluster that spirals in toward the *inner parsec* could have resulted in the bow-shock formation caused by the supersonic motion of the cluster, cluster stellar wind, NSC winds, and the ISM. The dense region in the bow-shock shell would then be the birthplace of the second generation of IRS 13 stars (see Table 9). We note that the S cluster (Eckart & Genzel 1996) exhibits a similar composition of stellar objects as listed in Table 9 (Habibi et al. 2017; Peißker et al. 2020c; Ciurlo et al. 2020; Peißker et al. 2021c, 2023a). However, one would naturally expect a certain degree of elongation for an extended structure that gravitationally interacts with an SMBH such as Sgr A* (see simulations of Hobbs & Nayakshin 2009; Jalali et al. 2014). While the dimensions and nature of IRS 13 will be the focus of Paper II, we want to note that the [Fe III] emission of the cluster implies a larger structure than is known from the literature. Considering the forbidden [Fe III] line distribution presented in Lutz et al. (1993), we find that the peak emission of the iron line clearly envelopes the IRS 13 and the IRS 2 region, suggesting a combined setup of the northern and southern cluster region (see Figure 14). It is already known that IRS 2C is a foreground star, while IRS 2L and IRS 2S are embedded in the dust feature associated with IRS 13 (Buchholz et al. 2013). However, our proposed interpretation of the dimensions of the cluster is in line with the polarization measurements of Buchholz et al. (2013) and Roche et al. (2018). The polarimetric and magnetic field line analysis of Roche et al. reveals that the dust feature, which envelopes IRS 13 and IRS 2L/2C, is a coherent structure. The line distribution of [Fe III] and the MIR dust emission match the size of the polarization region of IRS 13 in Buchholz et al. (2013) and Roche et al. (2018) underlying the proposed dimensions of the cluster in this work. In Paper II, we will present *N*-body simulations of an inspiraling cluster toward the *inner parsec* and investigate the possibility of such an event.

4.4. IRS 13 and the (counter-)clockwise disk

As we have shown in Figure 6, the investigated cluster member sample shows a nonuniform distribution. In addition, most of the stars in the NSC follow this nonisotropic kinematic pattern, which historically resulted in the finding of a counterclockwise and clockwise disk, abbreviated as CCWS and CWS respectively (Genzel et al. 1996; Paumard et al. 2006). The mentioned velocity pattern is characterized by the normalized angular momentum *j*, which is defined by Genzel et al. (2003) as

$$j = (xv_y - yv_x)/pv_p \tag{8}$$

where x, v_x, y, and v_y refer to RA and decl. coordinates and their related components of proper motion, respectively, while the total distance and proper motion are given by p and v_p. With the above equation and the numerical values given in Table 3, we find the same distribution (Figure 15) for IRS 13 sources as shown in Paumard et al. (2006). In analogy to the anisotropy parameter shown in Figure 6, we divide the data presented in Figure 15 into four bins. We estimate that the bin with $j \in \{0.5, 1.0\}$ contains 22% of the sources; for $j \in \{0.0, 0.5\}$, we get 8%; for $j \in \{0.0, -0.5\}$, there are 10% of the sources; and finally, for $j \in \{-0.5, -1.0\}$, we obtain 60%. Therefore, we find an overdensity in bin 4, which strengthens our result presented in Figure 6. Because a nonuniform cluster is supposed to peak at $\gamma_{TR} = \pm 1$ as shown in Figure 7,[11] it is expected to find anisotropic structures in the angular momentum plot displayed in Figure 15. For our sample, we clearly identify an overdensity at $j = -1$ (Figure 15), suggesting a CCW disk membership (Paumard et al. 2006; Ali et al. 2020; von Fellenberg et al. 2022). Based on this finding, we propose three different scenarios:

[10] See their Figure 10.

[11] In addition, Genzel et al. (2000) shows Monte Carlo simulations that demonstrate in agreement with our results that nonuniform cluster exhibits an overdensity of stars at $\gamma_{TR} = \pm 1$.

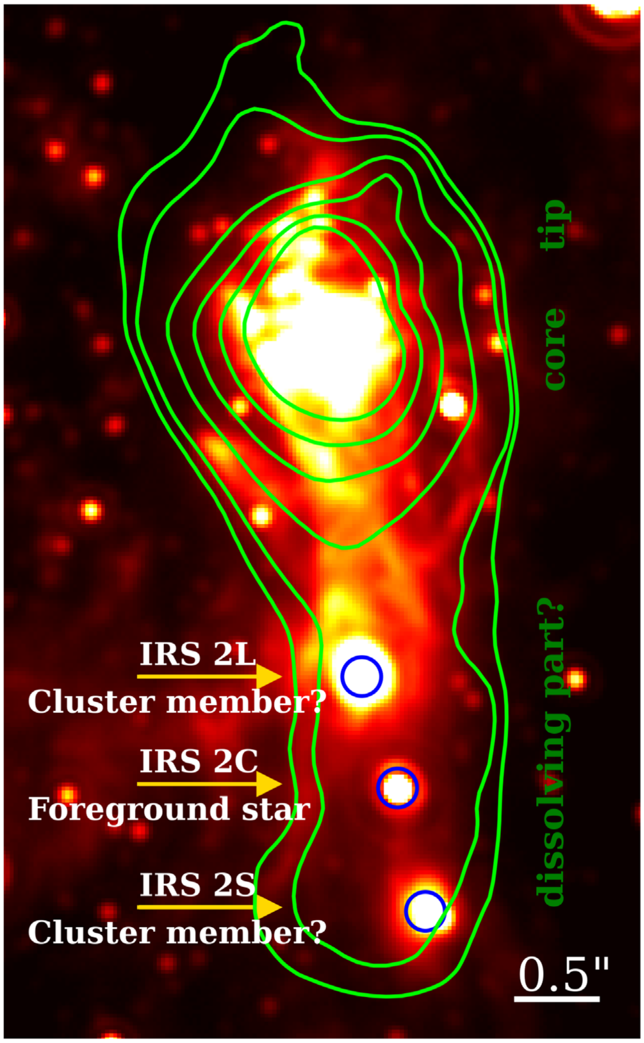

Figure 14. *L*-band NACO observation of IRS 13 in 2004 overlaid with [Fe III] 2.218 μm $^3G_5 \rightarrow ^3H_6$ contour lines extracted from a SINFONI 3D data cube. The contour lines represent the 26%, 30%, 40%, 50%, 60%, and 70% levels, whereas the peak emission is at 2.5×10^{-10}ergs^{-1}cm$^{-2}\mu$m^{-1}. The 70% contour line centered on the core region of IRS 13 resembles the projected size of the Hill radius (≈22m pc) estimated with Equation (7) in Section 3.2. In addition, the 30% contour lines enclose the southern region with respect to the core and tip components of the IRS 13 cluster. As indicated, we mark the two embedded sources, IRS 2L and IRS 2S, that might be former members of the core region of IRS 13. The compact source IRS 2C is also known as AF/AHH (Allen et al. 1990; Blum et al. 1996) and could be a foreground star based on the polarimetric analysis of Buchholz et al. (2013).

[a] The (C)CWS characterization of stars in the *inner parsec* is valid for all (gravitationally bound) subregions,
[b] The stellar overdensity of the IRS 13 cluster is the result of the intercepting disks of the CCW and CW systems,
[c] The IRS 13 cluster shows the imprint of the CCW and CW systems.

Concerning [a], we want to highlight the theoretical work of Hobbs & Nayakshin (2009), who predict two warped stellar disks/distributions for infalling molecular clouds. In addition, Ali et al. (2020) find a similar distribution for the S stars, which suggests that a two-disk or even a multidisk structure is present for other subregions as well, presumably those that are gravitationally bound to the SMBH or an IMBH. It needs to be verified by *N*-body numerical simulations how long the original disklike stellar structure that bears imprints of the

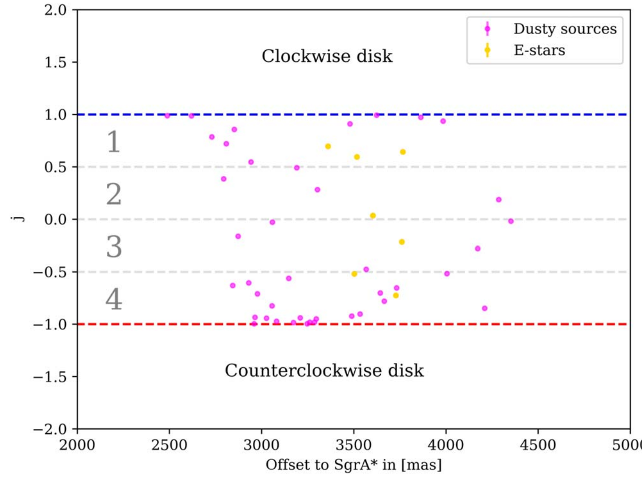

Figure 15. Normalized angular momentum *j* as a function of distance from Sgr A* for all the here investigated IRS 13 cluster members. We find a stellar distribution similar to the one derived by Paumard et al. (2006) for the majority of the NSC stars (see also von Fellenberg et al. 2022). Here, most of the investigated objects peak at $j = -1$, suggesting a CCW disk membership. Magenta circles represent the dusty sources analyzed in this work; the gold-filled ones indicate the E stars (Figure 3). The size of the individual data points covers up the uncertainties calculated with error propagation.

formation mechanism can survive within the NSC. As mentioned before, the results presented in Figure 15 do reveal that the majority of investigated cluster members (>50%) are part of at least one disk, presumably the CCW disk. In addition, Paumard et al. (2006) suggested that the IRS 13 cluster may result from the interaction of the CCW and CW disks, i.e., scenario [b]. Although this scenario cannot be excluded, it implies an underlining rotation pattern that may have been created by infalling clouds in the first place (see [a] and Hobbs & Nayakshin (2009)). Because the E stars seem to be members of both distributions (Figure 6, upper left plot), the scenario seems plausible. However, we will investigate this particular point in more detail in Paper II because it would exceed the scope of this work. For the last scenario, [c], the IRS 13 cluster serves as a tracer for the underlining disk pattern. The infalling cluster IRS 13 may have intercepted the CCW and CW disks, which led to compressed gas densities that triggered star formation. Likewise, for [b], we will focus on this point in Paper II. Independent of the exact relation between IRS 13 and the (C)CW disks, we want to stress that Hansen & Milosavljević (2003) demanded a second black hole of $\approx 10^4 M_\odot$ in order to explain the unusually young age of the S-cluster stars (Morris 1993; Ghez et al. 2003; Habibi et al. 2017). The mass estimate is in the same order as the estimated enclosed mass for IRS 13 of $3.9 \times 10^4 M_\odot$. Because of the age of the S-cluster members, IRS 13 is most certainly not a suitable candidate for process explaining the presence of young stars close to Sgr A*. But it is an interesting scientific question to explore and maybe even link possible large-scale imprints on molecular clouds in the circumnuclear disk (CND) from the enclosed mass of the IRS 13 cluster.

4.5. Multiplicity Fraction of the IRS 13 Cluster

Considering the young age of the IRS 13 cluster members, we should have detected an increased multiplicity and companion fraction (Portegies Zwart et al. 2010). Surprisingly, only one binary system close to IRS 13 is known (Pfuhl et al. 2014), which might not be related to the cluster in the first place. Taking into account the important role of binaries, especially for the evolution of massive stars (Sana et al. 2012), we expect frequent updates on the detection of binary systems in the IRS 13 cluster, particularly with the upcoming Extremely Large Telescope (ELT).

For example, Gautam et al. (2019) identified more than a dozen possible periodic systems. Because of resolution limitations, observation of visual binaries remains unlikely, damping the number of methods to detect such systems. Therefore, high-cadence observations with the scientific goal of identifying magnitude or line-of-sight (LOS) variations will remain the sufficient approach for multiplicity analysis.

However, given the number of sources investigated in this work, we speculatively expect at least one binary system among the sample. From the analysis, we observed minor position fluctuations of γ and ζ. These uncertainties may result from a confusion problem due to the high source density (Paumard et al. 2006).

Assuming that the above-mentioned uncertainties cannot be explained by source confusion, we will use the definition of Reipurth & Zinnecker (1993) and Duchêne et al. (2001) for the multiplicity fraction (MF) and the related companion fraction (CF). Consequently, MF is defined as

$$\mathrm{MF} = \frac{\mathrm{B + T + Q + \cdots}}{\mathrm{S + B + T + Q + \cdots}} \tag{9}$$

where S defines the number of single stars and B is the number of binary star systems. Triple and quadruple star systems are defined by T and Q letters in the above equation. In addition, CF can be written as

$$\mathrm{CF} = \frac{\mathrm{2B + 3T + 4Q + \cdots}}{\mathrm{S + 2B + 3T + 4Q + \cdots}} \tag{10}$$

and defines the ratio of stars with a companion. For simplicity, we assume that γ and ζ are two binary systems. In total, we derived seven orbital solutions for the brightest sources of the sample. These boundary conditions are translated to MF $\sim 28\%$ and CF $\sim 44\%$ using Equation (9) and Equation (10), respectively. If we assume a rough cluster age of 4 ± 1 Myr based on the most evolved E stars (Maillard et al. 2004; Paumard et al. 2006; Zhu et al. 2020), we find similar MF and CF values in other clusters with a comparable age, such as RCW 108 (Comerón et al. 2005; Comerón & Schneider 2007) and the SMC cluster NGC 330 (Bodensteiner et al. 2021). If these numbers hold, it would demonstrate comparable star formation channels between different (Galactic) clusters. We want to note that we assumed for the above discussion the presence of two unconfirmed binaries. However, we anticipate multiple opportunities for upcoming instruments and observation campaigns covering the IRS 13 cluster.

4.6. Observations with the James Webb Space Telescope

Despite strong indications for the nature of the dusty objects, the data lack detailed spectroscopic analysis. For YSOs of type I, we would typically use tracers such as H_2 (Glassgold et al. 2004), H_2O (Gibb et al. 2000), and HCN (Lahuis et al. 2006) to confirm the classification. Considering the recent start of the scientific operations of the James Webb Space Telescope, the upcoming guaranteed time observations (GTO)[12] of the GC will minimize the uncertainties of the YSO classification for the dusty sources. We note that there are publicly available archive[13] data observed with NIRSPEC in 2023. Consequently, we used this data set to inspect the spectral NIR emission and parts of the L band (MIR) for the presence of individual line tracers. Due to the absence of telluric emission/absorption lines, we find an unaffected Paα line but also strong water absorption features (Moultaka et al. 2015). With a nominal resolution power of ∼2700 with the G235H/F170LP setting, we identify several single emission and absorption lines (e.g., Brδ, HeI, Brγ, and CO band heads) in the H and K band that are well known from SINFONI observations of the same region (Peißker et al. 2020b, 2021a, 2023b). Considering the recent identification of snowlines in the spectrum of HH 48 NE, we expect similar findings in the GC with NIRSPEC in addition to YSO tracers that could potentially be identified with MIRI. Although the spatial L-band resolution of NACO and MIRI (JWST) is sufficiently comparable, a stable PSF and longer on-source integration times could result in new insights into the IRS 13 cluster. With the demonstrated capabilities of the JWST (Figure 16), we will search for tracers associated with YSOs (Peißker et al. 2023b). Because some dusty sources are close to the E stars, we aim to increase the number of cluster samples to verify our findings on the warped disk structure of IRS 13. In addition to the continuum detections presented in this work, we expect an increase in the number of line-emitting sources, such as G2/DSO (Peißker et al. 2021c), observed with the MIRI and NIRSPEC IFU data.

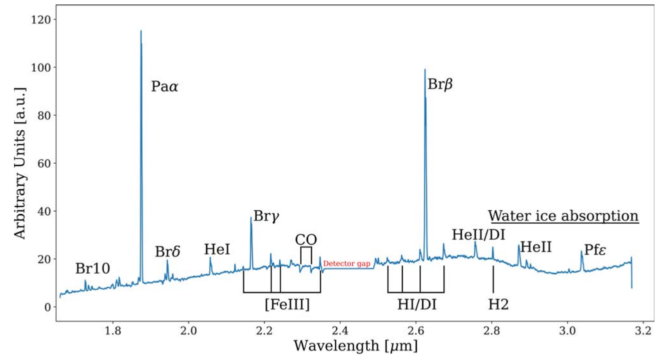

Figure 16. NIRSPEC spectrum of the *inner parsec* observed with the James Webb Space Telescope in 2022 (PI: Jessica Lu, Proposal ID: 1939). The NIRSPEC observation agrees with the water ice identification by, e.g., Moultaka et al. (2015). Around 2.4μm, the detector gap of NIRSPEC is marked.

5. Conclusions

We analyzed the IRS 13 cluster, which resides at a projected distance of ∼0.15 pc from Sgr A*. Based on the here presented work, we found a significantly higher number of cluster members of IRS 13 compared with previous studies. Using multiwavelength observations resulting in a comprehensive color–color diagram classification, we applied a ray-tracing radiative transfer model to investigate the nature of the brightest dusty sources and found compelling evidence that points toward a YSO characterization. The dusty sources share a comparable footprint with the bright dusty sources suggesting a YSO classification. In the following, we list our key findings:

[12] Prog. Id: GTO 1266.

[13] Downloaded from the Barbara A. Mikulski Archive for Space Telescopes (MAST).

1. The nature of the dusty objects can be described as MYSOs and HMYSOs in agreement with the classification of X3a,
2. Despite the low-mass YSO η, we classify all other investigated bright dusty sources as massive class I YSOs,
3. The majority of investigated sources in this work are arranged in a significant disk structure, presumably the CCW disk,
4. This nonuniform arrangement of the IRS 13 cluster is in remarkable agreement with previous normalized angular momentum studies of the NSC,
5. From the kinematics of the cluster members, we estimate a minimum mass of $4 \times 10^4 M_\odot$ that is required for a tidally stable system,
6. The derived tidal (Hill) radius shows a strong correlation with the dimensions of the peak emission distribution (dust/[Fe III]) of IRS 13 (Figure 14),
7. The tidally stable core of IRS 13 harbors massive O/WR stars but also HMYSOs,
8. In total, we find two generations of stellar objects that can be distinguished by their age.

In the future, we expect to identify more objects as the analyzed DS objects or the bow-shock source X3, which might be associated with the IRS 13 cluster. The large-scale MIRI (JWST) and ERIS (VLT) observations providing IFU data will enhance the characterization and the related precise stellar age determination of individual sources in the IRS 13 cluster.

Acknowledgments

We thank an anonymous referee for a constructive and encouraging report that helped to improve the manuscript. This work was supported in part by the Deutsche Forschungsgemeinschaft (DFG) via the Cologne Bonn Graduate School (BCGS), the Max Planck Society through the International Max Planck Research School (IMPRS) for Astronomy and Astrophysics, as well as special funds through the University of Cologne. Conditions and Impact of Star Formation is carried out within the Collaborative Research Centre 956, subproject [A02], funded by the Deutsche Forschungsgemeinschaft (DFG) project ID 184018867. M.Z. acknowledges the GAČR-LA grant No. GF23-04053L for financial support. Part of this work was supported by fruitful discussions with members of the European Union–funded COST Action MP0905: Black Holes in a Violent Universe and the Czech Science Foundation (No. 21-06825X). V.K. has been partially supported by the Czech Ministry of Education, Youth and Sports Research Infrastructure (LM2023047). A.P., J.C., S.E., and G.B. contributed useful points to the discussion. A.E. and F.P. acknowledge support through the German Space Agency DLR 50OS1501 and DLR 50OS2001 from 2015 to 2023. We also would like to thank the members of the SINFONI/NACO/VISIR and ESO's Paranal/Chile team for their support and collaboration. This paper makes use of the following ALMA data: ADS/JAO. ALMA # 2015.1.01080.S and ADS/JAO.ALMA # 2012.1.00543.S. ALMA is a partnership of ESO (representing its member states), NSF (USA), and NINS (Japan), together with NRC (Canada), MOST and ASIAA (Taiwan), and KASI (Republic of Korea), in cooperation with the Republic of Chile. The Joint ALMA Observatory is operated by ESO, AUI/NRAO, and NAOJ.

Facilities: VLT:Yepun, VLT:Antu, ALMA (Band 7).

Software: astropy (Astropy Collaboration et al. 2013, 2018, 2022), SciPy (Virtanen et al. 2020), Hyperion (Robitaille 2011, 2017), DPuser (Ott 2013).

Appendix

In this Appendix, we list the data used for the analysis. In addition, we compare the number of dusty sources of this work with the literature. We furthermore indicate the related proper motion of the sources investigated.

Appendix A
Data

In Table 10, we list the K-band data used in this work. Although the source confusion in the IRS 13 cluster is increased because of its high density, we identify K-band positions of the dusty objects in most epochs of the listed data.

Table 10
K-band Data Observed With NACO Between 2002 and 2018

NACO K-band		
Date	Observation ID	Number of exposures
2002.07.31	60.A-9026(A)	61
2003.06.13	713-0078(A)	253
2004.07.06	073.B-0775(A)	344
2004.07.08	073.B-0775(A)	285
2005.07.25	271.B-5019(A)	330
2005.07.27	075.B-0093(C)	158
2005.07.29	075.B-0093(C)	101
2005.07.30	075.B-0093(C)	187
2005.07.30	075.B-0093(C)	266
2005.08.02	075.B-0093(C)	80
2006.08.02	077.B-0014(D)	48
2006.09.23	077.B-0014(F)	48
2006.09.24	077.B-0014(F)	53
2006.10.03	077.B-0014(F)	48
2006.10.20	078.B-0136(A)	47
2007.03.04	078.B-0136(B)	48
2007.03.20	078.B-0136(B)	96
2007.04.04	179.B-0261(A)	63
2007.05.15	079.B-0018(A)	116
2008.02.23	179.B-0261(L)	72
2008.03.13	179.B-0261(L)	96
2008.04.08	179.B-0261(M)	96
2009.04.21	178.B-0261(W)	96
2009.05.03	183.B-0100(G)	144
2009.05.16	183.B-0100(G)	78
2009.07.03	183.B-0100(D)	80
2009.07.04	183.B-0100(D)	80
2009.07.05	183.B-0100(D)	139
2009.07.05	183.B-0100(D)	224
2009.07.06	183.B-0100(D)	56
2009.07.06	183.B-0100(D)	104
2009.08.10	183.B-0100(I)	62
2009.08.12	183.B-0100(I)	101
2010.03.29	183.B-0100(L)	96
2010.05.09	183.B-0100(T)	12
2010.05.09	183.B-0100(T)	24
2010.06.12	183.B-0100(T)	24
2010.06.16	183.B-0100(U)	48
2011.05.27	087.B-0017(A)	305
2012.05.17	089.B-0145(A)	169
2013.06.28	091.B-0183(A)	112
2017.06.16	598.B-0043(L)	36
2018.04.24	101.B-0052(B)	120

Table 11
L-band Data Observed With NACO Between 2002 and 2018

NACO *L*-band		
Date	Observation ID	Number of exposures
2002.08.30	060.A-9026(A)	80
2003.05.10	071.B-0077(A)	56
2004.07.06	073.B-0775(A)	217
2005.05.13	073.B-0085(E)	108
2005.06.20	073.B-0085(F)	100
2006.05.28	077.B-0552(A)	46
2006.06.01	077.B-0552(A)	244
2007.03.17	078.B-0136(B)	78
2007.04.01	179.B-0261(A)	96
2007.04.02	179.B-0261(A)	150
2007.04.02	179.B-0261(A)	72
2007.04.06	179.B-0261(A)	175
2007.06.09	179.B-0261(H)	40
2008.05.28	081.B-0648(A)	58
2008.08.05	179.B-0261(N)	64
2008.09.14	179.B-0261(U)	49
2009.03.29	179.B-0261(X)	32
2009.03.31	179.B-0261(X)	32
2009.04.03	082.B-0952(A)	42
2009.04.05	082.B-0952(A)	12
2009.09.19	183.B-0100(J)	132
2009.09.20	183.B-0100(J)	80
2010.07.02	183.B-0100(Q)	485
2011.05.25	087.B-0017(A)	29
2012.05.16	089.B-0145(A)	30
2013.05.09	091.C-0159(A)	30
2015.09.21	594.B-0498(G)	420
2016.03.23	096.B-0174(A)	60
2017.03.23	098.B-0214(B)	30
2018.04.22	0101.B-0065(A)	68
2018.04.24	0101.B-0065(A)	50

Table 12
SINFONI Data Used in This Work for the Identification of the Iron Line (see Figure 14)

Date (YYYY: MM:DD)	Observation ID	Exp. Time (s)	Band	Instrument/ Telescope
2014.08.30	093.B-0218(B)	2700	H + K	SINFONI/VLT

Note. We applied the standard reduction steps provided by the ESO pipeline to create the final mosaic.

In addition, the prominent MIR emission of these dusty sources enables us to incorporate all investigated epochs of the listed *L*-band data observed with NACO (see Table 11). The ID of the GC observation in the *H* and *K* band with SINFONI in 2014 is listed in Table 12.

Appendix B
Dusty objects

Here, we provide an overview of the sources investigated in this work compared with previous investigations in the literature. Table 13 exhibits all unknown and known dusty objects of the IRS 13 region with the corresponding ID of the related publication. To cross-identify all sources in the literature with this work, we visually compare finding charts of the related publication listed in Table 13. We expect that future higher-resolution observations will most certainly establish a new nomenclature as it is commonly done for GC sources (please compare the analysis of Eckart et al. 2013 with Ciurlo et al. 2020).

Table 13
Identification of All the Sources Investigated in This Work

ID	Maillard et al. (2004)	Schödel et al. (2005)	Mužić et al. (2008)	Fritz et al. (2010)	Eckart et al. (2013)
α			×		8
β			×		9
γ			×		22
δ			×		17
ϵ			×		13
ζ			×		34
η	15	×	×		19
ϑ					
ι		×			10
1		×	×		
2					
3					
4		×			
5					
6					
7					
8					
9		×			
10		×			
11	14	×	×		15
12	13	×	×		16
13					
14					
15					
16					
17	20	×	×		
18					
19					
20		×			
21					
22					23
23					
24	18	×			
25		×			
26			×		7
27	16		×		20
28					
29					
30					
31					
32					
33					
E1	×	×	×	×	1
E2	×	×	×	×	2
E3	×	×	×	×	3
E4	×	×		×	4
E5.0	×		×	×	5
E5.1				×	
E7	5	×	×	×	25

Note. As listed, the nomenclature is not consistent throughout the literature. A × symbol indicates the detection in the related publication. If the sources were labeled with an alternative ID, we additionally list the corresponding number.

Appendix C
Individual detections of the dusty sources

Here, we list all individual relative locations of the dusty sources investigated in this work. The related position of S2 is indicated. With the orbital elements of Do et al. (2019) and Gravity Collaboration et al. (2018), the position of Sgr A* can be estimated, which can be transferred to the absolute location of the dusty sources. The positions of the DS listed in Table 14 are determined using a Gaussian fit. In addition, this fit provides an uncertainty that is indicated after the related numerical RA and decl. value. From this table, the bulk motion of IRS 13 can be analyzed. Because this exceeds the scope of this work, we refer to Paper II for an extended analysis. Because of the consistency of the data set that transforms into a lowered confusion, we list the *L*-band positions in Table 14.

Table 14
Relative Pixel Positions of S2

Epoch	R.A.	err R.A.	Decl.	err Decl.
2002-08-29	685.59	0.02	764.57	0.02
2002-08-30	1121.1	0.03	787.88	0.03
2003-05-10	873.79	0.04	743.43	0.04
2004-04-25	678.01	0.07	640.11	0.05
2004-04-26	678.09	0.04	640.29	0.04
2005-05-13	788.84	0.06	776.4	0.05
2006-05-29	744.23	0.04	747.74	0.05
2007-04-01	1043.3	0.02	1050.8	0.02
2007-05-15	1040.2	0.06	1052.2	0.05
2007-05-16	1011.6	0.04	1074.3	0.04
2007-05-17	1038.9	0.08	1061.1	0.08
2007-05-18	1050.3	0.02	1051.	0.02
2007-05-19	972.05	0.05	1042.4	0.04
2007-05-22	808.75	0.02	812.64	0.02
2007-05-23	1057	0.03	1082.6	0.03
2008-05-26	1020	0.1	1110.9	0.1
2008-05-30	988.24	0.1	1100.9	0.1
2008-05-31	1049.2	0.1.	1070.8	0.1
2008-06-02	1056.8	0.1	1071.1	0.1
2008-06-03	1060.4	0.1	1072.2	0.1
2011-05-25	866.21	0.02	850.86	0.02
2012-05-16	867.6	0.04	787.45	0.04
2013-05-09	870.72	0.08	786.15	0.07
2016-03-23	847.81	0.05	826.22	0.04
2018-04-22	850.83	0.03	761.76	0.06
2018-04-24	852.93	0.03	758.05	0.04

Note. From the position of S2, the location of Sgr A* can be estimated. With this, the absolute positions of the dusty sources can be calculated. The uncertainties represent the Gaussian fit error. This table is for S2 only and the full table for all sources is available in machine-readable format with the online version of this article.

(This table is available in its entirety in machine-readable form.)

Appendix D
K-band counterpart of the dusty sources

Here, we display the *K*-band counterparts for dusty sources analyzed in this work. The *K*-band data presented in Figure 17 were observed in 2009 with NACO. Because of the proper motion of the DS, the detectability may be hindered for individual objects. Single detections of these objects, including light curves, are presented in Appendix F.

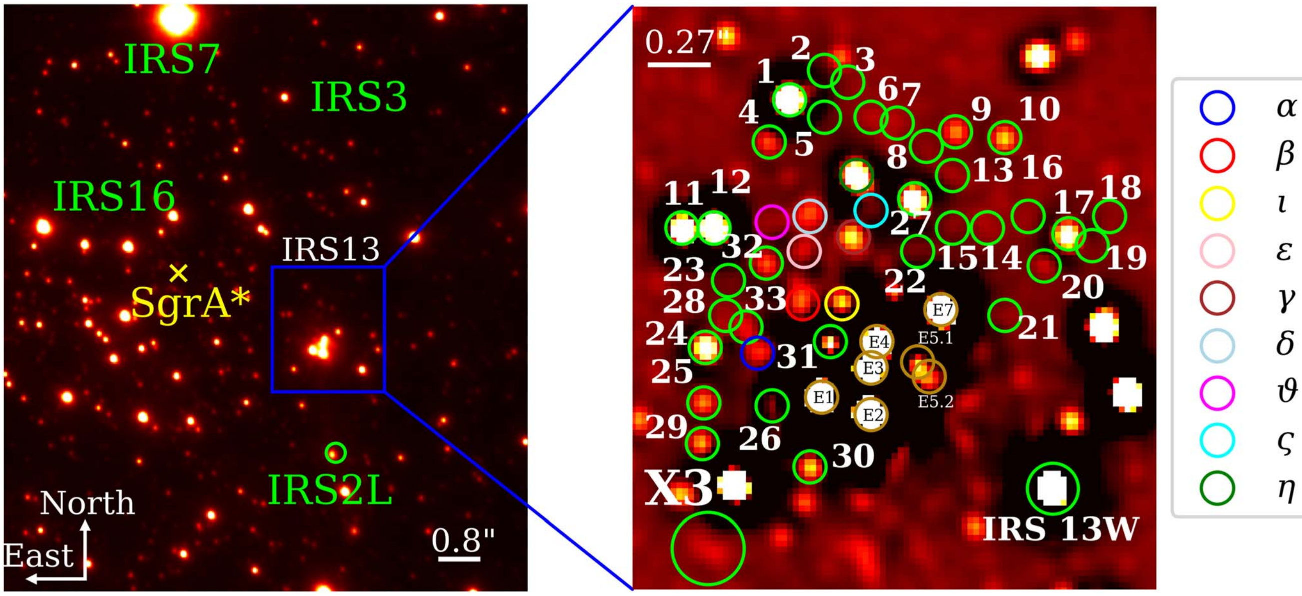

Figure 17. *K*-band observation of IRS 13 in 2009.

Appendix E
H-band counterpart of the dusty sources

Near-infrared NACO observations of the DS in the *H* band. The observations were carried out in 2004 and show the same field of view (FOV) as is presented in Figures 3 and 17. The detection of some sources in Figure 18 may be infected by confusion and interference, which is why we present individual detections in Appendix F.

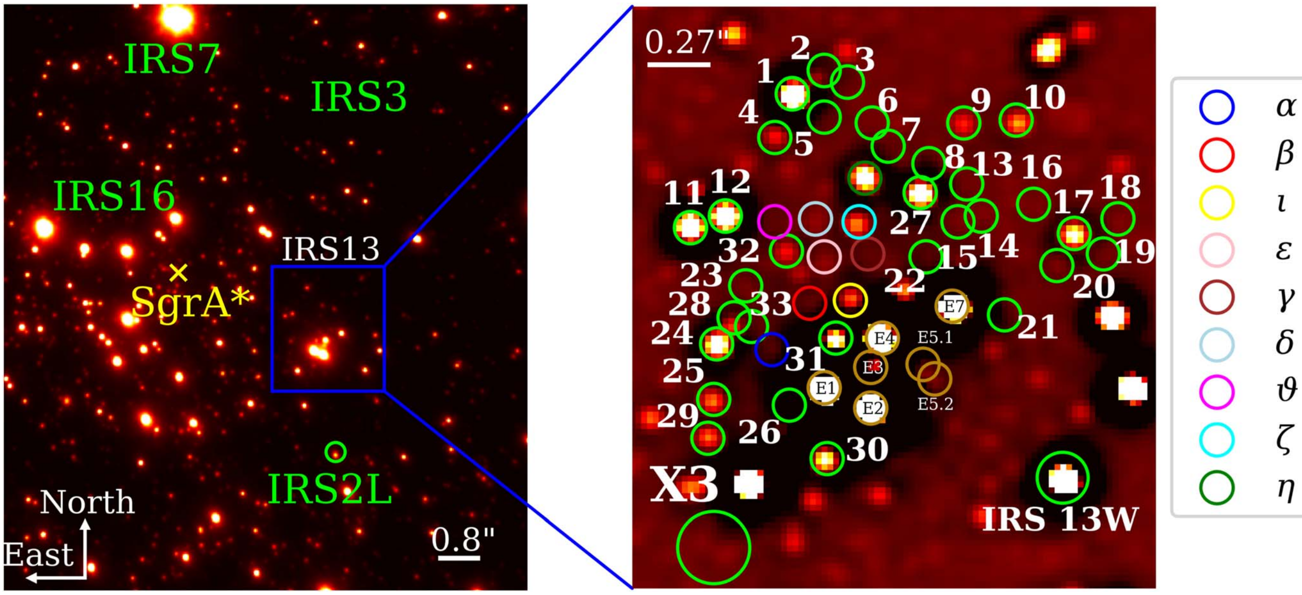

Figure 18. *H*-band observation of IRS 13 in 2004.

Appendix F
Multiwavelength identification of the dusty sources

We use the *L*-band emission presented in Figure 3 as a starting point to identify the here discussed dusty sources. Whenever feasible, we use the continuum data without any applied high-pass filter to detect the DS in the *H*, *K*, and *L* bands. Images and light curves based on the *H*-, *K*-, and *L*-band NACO data observed between 2002 and 2018 for the dusty sources DS1—DS33 are shown in Figure Set 19. In Table 15, we list mean and median magnitudes with the related standard deviations of DS1—DS33. For the photometric analysis, we use IRS 2L and S65 with an *L*-band magnitude of 10.59 ± 0.03 (Hosseini et al. 2020; Peißker et al. 2021a) as a calibrator. To determine the impact of the high-pass filter on the photometric analysis, we will compare the *L*-band magnitude of one of the brightest dusty sources, DS1, with and without the applied smooth-subtract algorithm.

As is demonstrated in Table 5, the impact on the magnitude after applying a high-pass filter is negligible. This result is expected because Ott et al. (1999) investigated the impact of applying different high-pass filters to the data in detail. The authors found no trend regarding a specific filter for almost 30 individual sources in agreement with the comparison presented in Table 5. Although individual sources may be affected by confusion, which is translated to brighter/fainter magnitude values, we note that nonfiltered data are exposed to crowding problems.

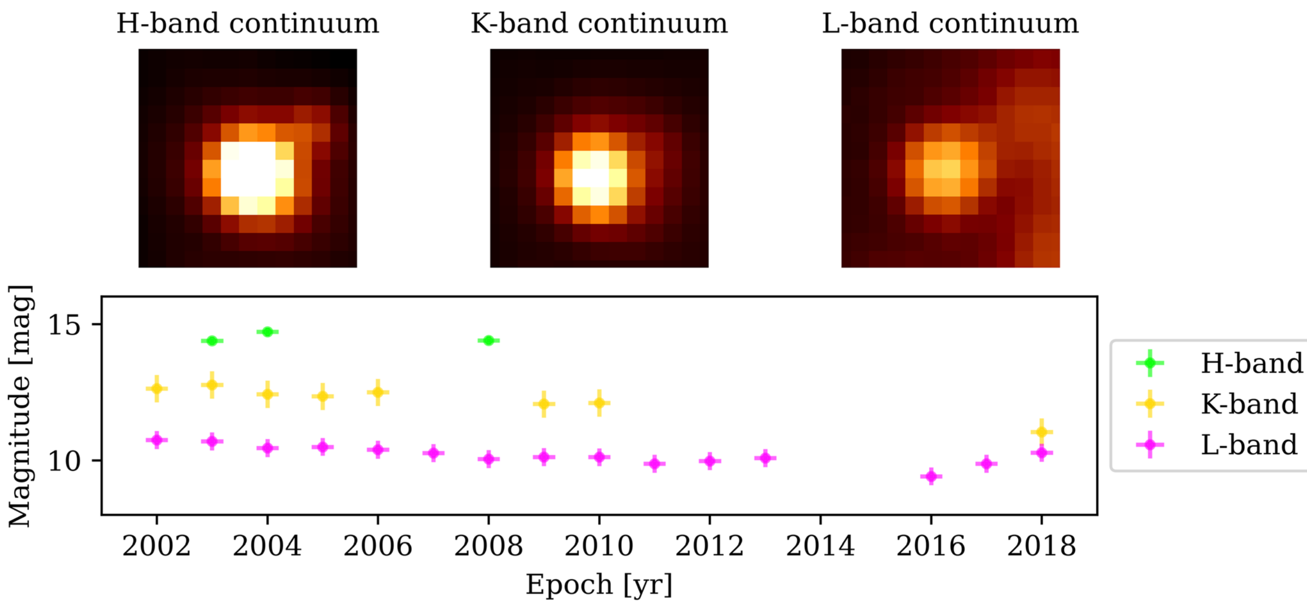

Figure 19. Multiwavelength identification of DS1 with NACO (see Figures 3, 18, and 17). The lower subplot displays the light curve with a fairly constant magnitude distribution between 2002 and 2018. The complete figure set, composed of 26 similarly arranged figures for DS1—DS33, is available in the online version of this article.

(The complete figure set (26 images) is available.)

Table 15
Estimated Magnitudes for DS1 Using Multiwavelength Observations Carried Out With NACO Between 2002 and 2018

	Mean	Median	STD
H band	14.40	14.49	0.15
K band	12.37	12.23	0.50
L band	10.13	10.19	0.33

Note. This table is for DS1 only; the full table for all dusty sources DS1—DS33 is available in machine-readable format with the online version of this article.

(This table is available in its entirety in machine-readable form.)

G.1. DS1

The source DS1 is one of the brightest *H*- and *K*-band objects of the here presented sample. In Figure Set 19, we show a confusion-free detection of DS1 in 2004.

G.2. DS2 & DS3

We do not detect a *K*- and *H*-band counterpart above the noise level for both sources, which is due to the high level of crowding. However, NACO *K*-band data of 2018 reveal some promising candidates that might be associated with DS2 and DS3.

G.3. DS4

Despite the close distance to DS1, the object DS4 can be observed without confusion. This object is a prime example of magnitude-confusion susceptibility; if the investigated object is bright enough, the close distance to a brighter object does not affect the observability. An example of a toxic magnitude-confusion susceptibility is displayed in the DS2 & DS3 detection in Figure Set 19.

G.4. DS5

The *L*-band detection of DS5 close to DS1. As for DS2 and DS3, the magnitude-confusion susceptibility is high, which might be the reason for the nondetection of DS5 in the *H* and *K* band. The classification of a coreless dust blob is rather unlikely because of evaporation timescales in a radiative-dominated environment. For example, Stewart et al. (2016) and Höfner & Freytag (2019) report variations of dust clouds close to stars on timescales of a few years.

G.5. DS6 & DS7

We identified DS6 in the *H*, *K*, and *L* band and DS7 in the *L* band. Close to DS6, a bright star is observable in the *H* and *K* band with no *L*-band counterpart, demonstrating the challenges of the multiwavelength analysis.

G.6. DS8

Like other fainter sources, the observation of DS8 is challenging because of the surrounding stars. While the *L*-band emission exhibits a low level of confusion, the detection of DS8 in the NIR bands is hindered by the presence of close-by stars.

G.7. DS9 & DS10

Because of their colors presented in Figure 9, DS9 and DS10 are most likely embedded stars, such as IRS 3. For cosmetic reasons, we use the *K*-band observation of 2009, which translates into a minor offset compared with the *H*- and *L*-band data from 2004. This apparent misalignment is not in conflict with the overall identification of the two stars.

G.8. DS11 & DS12

As for DS9 and DS10, we use *K*-band data of 2009 to complement the observations in the *H* and *L* band of 2004. Both sources, DS11 and DS12, can be most likely classified as stellar sources encircled by a dusty envelope.

G.9. DS13

For DS13, we note an increased magnitude-confusion susceptibility throughout the accessible IR bands. The observation of fainter DS sources is even more challenging because of the high stellar density.

G.10. DS14 & DS15

Both sources, DS14 and DS15, are detected in the *H*, *K*, and *L* band but suffer from increased confusion. In Figure Set 19, we show data observed in 2004 (*H* and *L* band) and 2009 (*K* band). The *K*-band detection of DS15 is especially exposed to the dominant emission of close-by stars, including their respective PSF wings. Despite these challenges, we managed to estimate the *K*-band magnitude of DS15 for several epochs as indicated in the light curve.

G.11. DS16 & DS17

While we identified a confusion-free detection of DS17, the close-by and fainter object DS16 experiences the dominant imprint surrounding stars. As for DS14 and DS15, we use data from 2004 (*H* and *L* band) and 2009 (*K* band) for cosmetic reasons. The detection of DS16 especially demonstrates the challenges of this analysis. While the observation of DS16 is confusion-free in the *L* band, the detection in the NIR bands requires the astrometric identification in the MIR band to avoid a false association.

G.12. DS18 & DS19

Because of the close distance to the bright star DS17, the detection of DS18 and DS19 is hindered. Hence, the magnitude-confusion susceptibility is increased.

G.13. DS20

For DS20, we do not find increased confusion due to crowding. The magnitude-confusion susceptibility is lowered.

G.14. DS21

The source DS21 is close to the E star E7. Because of the bright emission of the E stars, the source suffers from blending and dominant PSF wings, although DS21 seems isolated. Despite the challenges of the identification related to DS21, we identify the source in several epochs.

G.15. DS22

The detection of DS22 in the *H* and *K* band is challenging because of the close distance of several surrounding stars. As demonstrated for DS20, the close distance of bright stars does not have to result in lowered detectability. However, because of the low *K*- and *H*-band magnitude of DS22, the detection of the source is limited to a few epochs.

G.16. DS23

Like DS22, the source DS23 suffers from close-by stars and increased confusion.

G.17. DS24

The bright source is at the eastern edge of the IRS 13 cluster and, therefore, is not affected by the dominant crowding of the inner core region. We detect DS24 without confusion in various epochs.

G.18. DS25

Like DS24, the source DS25 is at the edge of the cluster. The chance for confusion is lowered, which is why we detect the source in all analyzed bands.

G.19. DS26

The source DS26 is affected by the dominant PSF wings of E1, the O supergiant in the core of IRS 13. Therefore, the detection of DS26 is limited to a few epochs.

G.20. DS27

The bright source DS27 can be observed without confusion in the available data set covering the epochs between 2002 and 2018.

G.21. DS28

The source DS28 is at the northern tip of an apparent elongated *L*-band feature consisting of DS31 and DS33. We detect DS28 without confusion in several bands and epochs.

G.22. DS29

The source DS29 is on a north–south axis with DS24 and DS25. Like the former two sources, DS29 is at the edge of the IRS 13 cluster and north of X3 (Peißker et al. 2023b). We detect DS29 without confusion.

G.23. DS30

Like DS26, the source DS30 is close to the E star E1. Because of the brightness of DS30, we detect the source without confusion in various epochs.

G.24. DS31

The source DS31 suffers, like, for example, DS26, from the toxic imprint of the core stars of the IRS 13 cluster. This is reflected by a variation of the magnitude in various bands. The significance of the detection is lowered because the variation of the individual magnitude values is partially outside the range of the standard deviation.

G.25. DS32

The source DS32 is close to the brighter dusty sources of the IRS 13 cluster. Although the chance of confusion is increased by the amount of close-by stars, we detect DS32 in all epochs between 2002 and 2018.

G.26. DS33

As mentioned before, the location of DS33 can be associated with an elongated *L*-band feature (DS28). However, this feature is most likely a chance association because we identify the individual components as DS sources.

ORCID iDs

Florian Peißker https://orcid.org/0000-0002-9850-2708
Michal Zajaček https://orcid.org/0000-0001-6450-1187
Andreas Eckart https://orcid.org/0000-0001-6049-3132
Lucas Labadie https://orcid.org/0000-0001-5342-5713
Vladimír Karas https://orcid.org/0000-0002-5760-0459
Nadeen B. Sabha https://orcid.org/0000-0001-7134-9005
Lukas Steiniger https://orcid.org/0000-0002-5859-3932
Maria Melamed https://orcid.org/0000-0002-4902-3794

References

Ali, B., Paul, D., Eckart, A., et al. 2020, ApJ, 896, 100
Astropy Collaboration, Price-Whelan, A. M., Lim, P. L., et al. 2022, ApJ, 935, 167
Astropy Collaboration, Price-Whelan, A. M., Sipőcz, B. M., et al. 2018, AJ, 156, 123
Astropy Collaboration, Robitaille, T. P., Tollerud, E. J., et al. 2013, A&A, 558, A33
Allen, D. A., Hyland, A. R., & Hillier, D. J. 1990, MNRAS, 244, 706
Baumgardt, H., Amaro-Seoane, P., & Schödel, R. 2018, A&A, 609, A28
Beckwith, S. V. W., Sargent, A. I., Chini, R. S., & Guesten, R. 1990, AJ, 99, 924
Berrilli, F., Corciulo, G., Ingrosso, G., et al. 1992, ApJ, 398, 254
Bhat, H. K., Sabha, N. B., Zajaček, M., et al. 2022, ApJ, 929, 178
Blum, R. D., Sellgren, K., & Depoy, D. L. 1996, ApJ, 470, 864
Bodensteiner, J., Sana, H., Wang, C., et al. 2021, A&A, 652, A70
Bonnet, H., Abuter, R., Baker, A., et al. 2004, Msngr, 117, 17
Brinch, C., Crapsi, A., Hogerheijde, M. R., & Jørgensen, J. K. 2007, A&A, 461, 1037
Buchholz, R. M., Witzel, G., Schödel, R., & Eckart, A. 2013, A&A, 557, A82
CASA Team, Bean, B., Bhatnagar, S., et al. 2022, PASP, 134, 114501
Chiang, E. I., & Goldreich, P. 1997, ApJ, 490, 368
Ciurlo, A., Campbell, R. D., Morris, M. R., et al. 2020, Natur, 577, 337
Clénet, Y., Rouan, D., Gratadour, D., Gendron, E., & Lacombe, F. 2003, in SF2A-2003: Semaine de l'Astrophysique Francaise, ed. F. Combes et al. (Les Ulis: EDP Sciences), 163
Clénet, Y., Rouan, D., Gratadour, D., Gendron, E., & Lacombe, F. 2005, in Proc. ESO Workshop, Science with Adaptive Optics, ed. W. Brandner & M. E. Kasper (Berlin: Springer), 286
Comerón, F., & Schneider, N. 2007, A&A, 473, 149
Comerón, F., Schneider, N., & Russeil, D. 2005, A&A, 433, 955
Davies, R., Esposito, S., Schmid, H. M., et al. 2018, Proc. SPIE, 10702, 1070209
Do, T., Hees, A., Ghez, A., et al. 2019, Sci, 365, 664
Draine, B. T. 2003, ARA&A, 41, 241
Duchêne, G., Simon, T., Eislöffel, J., & Bouvier, J. 2001, A&A, 379, 147
Eckart, A., & Genzel, R. 1996, Natur, 383, 415
Eckart, A., & Genzel, R. 1997, MNRAS, 284, 576
Eckart, A., Hüttemann, A., Kiefer, C., et al. 2017, FoPh, 47, 553
Eckart, A., Moultaka, J., Viehmann, T., Straubmeier, C., & Mouawad, N. 2004, ApJ, 602, 760
Eckart, A., Mužić, K., Yazici, S., et al. 2013, A&A, 551, A18
Eisenhauer, F., Abuter, R., Bickert, K., et al. 2003, Proc. SPIE, 4841, 1548
Event Horizon Telescope Collaboration, Akiyama, K., Alberdi, A., et al. 2022, ApJL, 930, L12
Fritz, T. K., Gillessen, S., Dodds-Eden, K., et al. 2010, ApJ, 721, 395
Fritz, T. K., Gillessen, S., Dodds-Eden, K., et al. 2011, ApJ, 737, 73
Gravity Collaboration, Abuter, R., Amorim, A., et al. 2018, A&A, 615, L15
Gautam, A. K., Do, T., Ghez, A. M., et al. 2019, ApJ, 871, 103
Genzel, R. 2022, RvMP, 94, 020501
Genzel, R., Pichon, C., Eckart, A., Gerhard, O. E., & Ott, T. 2000, MNRAS, 317, 348
Genzel, R., Schödel, R., Ott, T., et al. 2003, ApJ, 594, 812
Genzel, R., Thatte, N., Krabbe, A., Kroker, H., & Tacconi-Garman, L. E. 1996, ApJ, 472, 153
Ghez, A. M., Duchêne, G., Matthews, K., et al. 2003, ApJL, 586, L127
Gibb, E. L., Whittet, D. C. B., Schutte, W. A., et al. 2000, ApJ, 536, 347
Gillessen, S., Genzel, R., Fritz, T. K., et al. 2012, Natur, 481, 51
Glassgold, A. E., Najita, J., & Igea, J. 2004, ApJ, 615, 972
Habibi, M., Gillessen, S., Martins, F., et al. 2017, ApJ, 847, 120
Hansen, B. M. S., & Milosavljević, M. 2003, ApJL, 593, L77
Hobbs, A., & Nayakshin, S. 2009, MNRAS, 394, 191
Höfner, S., & Freytag, B. 2019, A&A, 623, A158
Hosseini, S. E., Zajaček, M., Eckart, A., Sabha, N. B., & Labadie, L. 2020, A&A, 644, A105

Ishii, M., Nagata, T., Sato, S., et al. 1998, AJ, 116, 868
Ito, M., Yamashita, T., Sako, S., et al. 2008, ApJ, 672, 398
Ivezic, Z., Nenkova, M., & Elitzur, M. 1999, DUSTY: Radiation transport in a dusty environment, Astrophysics Source Code Library, ascl:9911.001
Jalali, B., Pelupessy, F. I., Eckart, A., et al. 2014, MNRAS, 444, 1205
Kenyon, S. J., & Hartmann, L. 1995, ApJS, 101, 117
Kozasa, T., & Sogawa, H. 1999, in IAU Symp. 191, Asymptotic Giant Branch Stars, ed. T. Le Bertre, A. Lebre, & C. Waelkens (Cambridge: Cambridge Univ. Press), 239
Lada, C. J. 1987, in IAU Symp. 115 (Cambridge: Cambridge Univ. Press), 1
Lada, C. J., & Adams, F. C. 1992, ApJ, 393, 278
Lahuis, F., van Dishoeck, E. F., Boogert, A. C. A., et al. 2006, ApJL, 636, L145
Leinert, C., Graser, U., Przygodda, F., et al. 2003, Ap&SS, 286, 73
Lenzen, R., Hartung, M., Brandner, W., et al. 2003, Proc. SPIE, 4841, 944
Lu, J. R., Do, T., Ghez, A. M., et al. 2013, ApJ, 764, 155
Lucy, L. B. 1974, AJ, 79, 745
Lutz, D., Krabbe, A., & Genzel, R. 1993, ApJ, 418, 244
Maillard, J. P., Paumard, T., Stolovy, S. R., & Rigaut, F. 2004, A&A, 423, 155
Martín, S., Martín-Pintado, J., Montero-Castaño, M., Ho, P. T. P., & Blundell, R. 2012, A&A, 539, A29
Menten, K. M., Reid, M. J., Eckart, A., & Genzel, R. 1997, ApJL, 475, L111
Moneti, A., Cernicharo, J., & Pardo, J. R. 2001, ApJL, 549, L203
Morris, M. 1993, ApJ, 408, 496
Moser, L., Sánchez-Monge, Á., Eckart, A., et al. 2017, A&A, 603, A68
Moultaka, J., Eckart, A., & Mužić, K. 2015, ApJ, 806, 202
Murray-Clay, R. A., & Loeb, A. 2012, NatCo, 3, 1049
Mužić, K., Eckart, A., Schödel, R., et al. 2010, A&A, 521, A13
Mužić, K., Schödel, R., Eckart, A., Meyer, L., & Zensus, A. 2008, A&A, 482, 173
Ojha, D. K., Tamura, M., Nakajima, Y., et al. 2009, ApJ, 693, 634
Ott, T. 2013, DPUSER: Interactive language for image analysis, Astrophysics Source Code Library, ascl:1303.025
Ott, T., Eckart, A., & Genzel, R. 1999, ApJ, 523, 248
Parsa, M., Eckart, A., Shahzamanian, B., et al. 2017, ApJ, 845, 22
Paumard, T., Genzel, R., Martins, F., et al. 2006, ApJ, 643, 1011
Peißker, F., Ali, B., Zajaček, M., et al. 2021a, ApJ, 909, 62
Peißker, F., Eckart, A., Sabha, N. B., Zajaček, M., & Bhat, H. 2020b, ApJ, 897, 28
Peißker, F., Eckart, A., Zajaček, M., & Britzen, S. 2022, ApJ, 933, 49
Peißker, F., Hosseini, S. E., Zajaček, M., et al. 2020c, A&A, 634, A35
Peißker, F., Zajaček, M., Eckart, A., et al. 2019, A&A, 624, A97
Peißker, F., Zajaček, M., Eckart, A., et al. 2021c, ApJ, 923, 69
Peißker, F., Zajaček, M., Eckart, A., et al. 2023a, ApJ, 943, 183
Peißker, F., Zajaček, M., Sabha, N. B., et al. 2023b, ApJ, 944, 231
Pfuhl, O., Alexander, T., Gillessen, S., et al. 2014, ApJ, 782, 101
Portegies Zwart, S. F., & McMillan, S. L. W. 2002, ApJ, 576, 899
Portegies Zwart, S. F., McMillan, S. L. W., & Gieles, M. 2010, ARA&A, 48, 431
Pott, J. U., Eckart, A., Glindemann, A., et al. 2008, A&A, 480, 115
Reipurth, B., & Zinnecker, H. 1993, A&A, 278, 81
Rieke, G. H., & Lebofsky, M. J. 1985, ApJ, 288, 618
Robitaille, T. P. 2011, A&A, 536, A79
Robitaille, T. P. 2017, A&A, 600, A11
Roche, P. F., Lopez-Rodriguez, E., Telesco, C. M., Schödel, R., & Packham, C. 2018, MNRAS, 476, 235
Rousset, G., Lacombe, F., Puget, P., et al. 2003, Proc. SPIE, 4839, 140
Sana, H., de Mink, S. E., de Koter, A., et al. 2012, Sci, 337, 444
Schödel, R., Eckart, A., Iserlohe, C., Genzel, R., & Ott, T. 2005, ApJL, 625, L111
Schödel, R., Merritt, D., & Eckart, A. 2009, A&A, 502, 91
Schödel, R., Morris, M. R., Muzic, K., et al. 2011, A&A, 532, A83
Scoville, N., & Burkert, A. 2013, ApJ, 768, 108
Scoville, N. Z., Stolovy, S. R., Rieke, M., Christopher, M., & Yusef-Zadeh, F. 2003, ApJ, 594, 294
Shahzamanian, B., Eckart, A., Zajaček, M., et al. 2016, A&A, 593, A131
Shahzamanian, B., Schödel, R., Nogueras-Lara, F., et al. 2022, A&A, 662, A11
Sicilia-Aguilar, A., Banzatti, A., Carmona, A., et al. 2016, PASA, 33, e059
Stewart, P. N., Tuthill, P. G., Monnier, J. D., et al. 2016, MNRAS, 455, 3102
Tsuboi, M., Kitamura, Y., Tsutsumi, T., et al. 2017a, ApJL, 850, L5
Tsuboi, M., Kitamura, Y., Tsutsumi, T., et al. 2019, PASJ, 71, 105
Tsuboi, M., Kitamura, Y., Tsutsumi, T., et al. 2020a, PASJ, 72, 36
Tsuboi, M., Kitamura, Y., Tsutsumi, T., et al. 2020b, PASJ, 72, L5
Tsuboi, M., Kitamura, Y., Uehara, K., et al. 2017b, ApJ, 842, 94
Tsuchikawa, T., Kaneda, H., Oyabu, S., et al. 2021, A&A, 651, A117
Tursunov, A., Zajaček, M., Eckart, A., et al. 2020, ApJ, 897, 99
Ulrich, R. K. 1976, ApJ, 210, 377
Viehmann, T. 2007, PhD thesis, Univ. Cologne
Viehmann, T., Eckart, A., Schödel, R., Pott, J. U., & Moultaka, J. 2006, ApJ, 642, 861
Virtanen, P., Gommers, R., Oliphant, T. E., et al. 2020, NatMe, 17, 261
von Fellenberg, S. D., Gillessen, S., Stadler, J., et al. 2022, ApJL, 932, L6
Wang, Q. D., Li, J., Russell, C. M. P., & Cuadra, J. 2020, MNRAS, 492, 2481
Weingartner, J. C., & Draine, B. T. 2001, ApJS, 134, 263
Witzel, G., Ghez, A. M., Morris, M. R., et al. 2014, ApJL, 796, L8
Zajaček, M., Britzen, S., Eckart, A., et al. 2017, A&A, 602, A121
Zajaček, M., Karas, V., & Eckart, A. 2014, A&A, 565, A17
Zhu, Z., Li, Z., Ciurlo, A., et al. 2020, ApJ, 897, 135
Zubko, V., Dwek, E., & Arendt, R. G. 2004, ApJS, 152, 211